



UNIVERSITY OF
BIRMINGHAM

**Two case studies of SPH modelling in biological
system:**

Large intestine and Deep vein valves

by

WEI WEN

A thesis submitted to

The University of Birmingham

for the degree of

MASTER OF PHILOSOPHY

School of Chemical Engineering

College of Engineering and Physical Sciences

The University of Birmingham

May 2018

UNIVERSITY OF
BIRMINGHAM

University of Birmingham Research Archive

e-theses repository

This unpublished thesis/dissertation is copyright of the author and/or third parties. The intellectual property rights of the author or third parties in respect of this work are as defined by The Copyright Designs and Patents Act 1988 or as modified by any successor legislation.

Any use made of information contained in this thesis/dissertation must be in accordance with that legislation and must be properly acknowledged. Further distribution or reproduction in any format is prohibited without the permission of the copyright holder.

ABSTRACT

Computational Fluid Dynamics (CFD) techniques has proven its adaptiveness and mutuality in various application for diversified fields. At the moment, the investigation of physical mechanics developed by CFD in physiological transportation has captured great attention. This thesis aims at deepening the insight into the interactive mechanism between the periodic deformable human conduits and the conveyed fluid content. The adopted models are not striving for the complete consistency with the real physiological conditions, and thus they are simplified and characterized by certain physical properties, such as the pressure, velocity and stress. First of all, a coupled method consists of Smoothed Particle Hydrodynamics (SPH) method and Coarse-Grained Molecular Dynamics (CGMD) / Mass-spring modelling (MSM) is adopted as it has proven its potentials in dealing with the transportation inside the deformable solid boundaries. The fluid part is simply simulated by the SPH method while the soft solid boundaries are mimicked by another method used in the coupled approach to yield the optimal utility of the coupled method. The models developed for Gastric Intestine (GI) system are first validated by comparisons with PET (Positron Emission Tomography) experimental outcomes. Quantitative analysis is made among simulations to illustrate the mixing and transportation of food propelled by the muscle peristalsis. Then the method is further extended into the study of the venous system and the results indicate a good interpretation of the pathological study of the valve dysfunction and the venous development.

Acknowledge

Firstly, I want to express my great gratitude to my supervisor Prof. Mostafa Barigou for offering me this precious opportunity to work with him. I have not only received valuable academic guidance from him but also learned a lot from his attitude towards life and research, which really gives me immense help especially at the time when I am stuck in the deep depression and my family issues. I would also like to thank Dr. Alessio Alexiadis, for his tutorial advice and elaborate assistance, he gives me the detailed introduction to coding and patient help through my research, which exceeds my estimate by a great deal. I feel it is a great fortune to have such nice supervisors and they are not just supervisors on my research, but also the life mentors help me to stand up from the bottom in my life.

I would like to thank my colleagues, Dr. Shuai Tian for his valuable suggestion and advice through my early research times; to Shahad Al-Najjar and Zainab Al-sharify for regular communication about modelling and data processing, especially much thanks to Mostapha Araine for the detailed discussions about the model modification and invaluable suggestions on my thesis writing.

I really appreciate the staff from the General Office, especially Lynn Draper, she tries her best to offer me continuous and thoughtful help, and I will always remember her kindness.

I would like to thank my warm-hearted suggestion form Dr. Shangfeng Du and staff from Embassy of the United Kingdom.

I would like to thank my friends, Xiaotong Zhang, Yaxiang Lu, Cong Sui, Yu Liu, Anqi Wang, Mingming Du, Dandan Zhang, Rui Wang, Qinghua Yu, Hong Xiao, Chuan Li for their friendship, it is a great pleasure to make acquaintances with them.

I would like to express my thanks to my family for their endless support and patient encouragement. They lead me to reconstruct my self-esteem and help me to control my mind and my life myself. Their infinite care and warm comfort is the most effective antidepressant Prozac pills I have ever taken. I don't know how long will be to fight with depressive disorder, but I know I won't give up since I have such a warm family still waits my support.

In conclusion, I want to dedicate my thesis to my mother, she is the Wonder Woman in my life and always redeems my heart and mind. My only and best wish is a stable and gradual recovery for her.

TABLE OF CONTENT

Chapter 1 Introduction	1
1.1 Project Background.....	1
1.2 CFD applications for mathematical modelling of human physiology	3
1.3 Project objectives	5
1.4 Thesis Layout	7
Chapter 2 Literature Review	9
2.1 Introduction.....	9
2.2 Basic SPH concept.....	12
2.2.1 Integral approximation	12
2.2.2 Particle approximation	15
2.2.3 Kernel function	16
2.3 Governing equations	18
2.3.1 The momentum equation.....	19
2.3.2 The continuity equation.....	20
2.3.3 The viscous term	21
2.3.4 Equation of state and artificial compressibility	24
2.4 Boundary treatment.....	25
2.5 Coarse-Grained Molecular Dynamics (CGMD) / Mass-spring modelling (MSM) ..	26
2.6 Coupling the two models/ discrete multi-hybrid system (DMHS).....	27
2.7 Benchmark verification	29
2.7.1 The basic structure of the simulation	29
2.7.2 General description of two cases	31
2.7.2 The specific treatment of the simulations.....	32
2.7.3 Validation against theoretical solutions	35
2.8 Conclusions.....	37
Chapter 3	38
SPH simulation of hydrodynamics within the GI tract using LAMMPS.....	38
Abstract	38
3.1 Introduction.....	39

3.2 Modelling.....	41
3.2.1 Modelling approach	41
3.2.1 Specific parameters used in DMHS method intestine simulation.....	42
3.2.2 Geometry.....	43
3.2.3 Peristaltic wave	46
3.2.4 Preliminaries and dimensionless analysis	49
3.3 Results.....	51
3.3.1 Simulations.....	51
3.3.2 Validation.....	52
3.3.3 Method for calculating the front velocity (u_F) from the simulations	54
3.4 Discussion	55
3.4.1 Pouring Mode.....	56
3.4.2 Surfing mode.....	58
3.4.3 Ineffective surfing mode	59
3.4.4 The dominant mode.....	61
3.5. Conclusions	66
Chapter 4	68
SPH simulation of hydrodynamics within the deep vein valves using LAMMPS	68
Abstract	68
4.2 Modelling	72
4.2.1 Modelling approach	72
4.2.2 Geometry.....	73
4.3 Parameters for simulations in DMHS method.....	75
4.4 Results and discussion	79
4.4.1 Force and velocity results.....	79
4.4.2 Mechanical stress	80
4.4.3. Retention time in the sinus.....	82
4.4.4 Parametric study.....	83
4.5. Agglomeration	90
4.6 Conclusions	92
Chapter 5	94

Conclusions and Future Work.....	94
5.1 Conclusions.....	94
5.1.1 Modelling of intestine segments by DMHS method.....	94
5.1.1 Modelling of venous valves by DMHS method.....	95
5.2 Future recommendations	97
Reference.....	99

LIST OF FIGURES

Figure. 2.1 Standard solution process for coupled molecular method.....	30
Figure. 2.2 Initial geometrical treatment for the simulation of Poiseuille flow and Couette flow	34
Figure. 2.3 Fluid particle distribution for (a)Poiseuille flow and (b)Couette flow at 10000-th step.....	35
Figure.2.4 Fluid particle velocity profiles for (a)Poiseuille flow and (b)Couette flow at $t=0.01s, 0.1s, \infty$	36
Figure. 3.1 The geometry used in the simulation (a), the contraction of the	45
Figure. 3.2 Schematic representation of the progressive contractions and expansion of the membrane sections during the peristaltic wave.....	47
Figure. 3.3 Simulation snapshots illustrating the fluid motion induced by a peristaltic wave for $v = 10^{-6} \text{ m}^2 \text{ s}^{-1}$, $L = 1.11 \text{ cm}$ and $V_w = 1.45 \text{ cm s}^{-1}$. The tracking (white) particles partially mix with the fluid of other pockets (pouring mode) and partially advance on the surface of the channel (surfing mode). The fluid that moved in the second pocket at t_w partially flows back into the first pocket at $3t_w$ (ineffective surfing). See Section 2.4 for details on these three propagation modes.....	49

Figure. 3.4 PET images: greyscale distribution plots (b), generated from the experimental data (a), compared to dimensionless concentration N/N_0 of tracker particles in the simulations (c) after 5 and 7 peristaltic waves ($\nu = 10^{-6} \text{ m}^2 \text{ s}^{-1}$, $L = 0.8 \text{ cm}$, $V_w = 1.45 \text{ cm s}^{-1}$). The concentration N_0 in the first pocket has been normalized to match the experiments and the distribution rescaled accordingly. Units between (b) and (c) are therefore different. Distributions (b) are continuous and indicate the tracer concentration along the whole channel. Distributions (c) are discrete and indicate the concentration of white particles in each pocket.53

Figure. 3.5 Front penetration x_F versus time for the cases: $L = 0.46 \text{ cm}$ $\nu = 2 \cdot 10^{-6} \text{ m}^2 \text{ s}^{-1}$, $V_w = 1.45 \text{ cm s}^{-1}$ (a), $L = 0.81 \text{ cm}$ $\nu = 1.6 \cdot 10^{-6} \text{ m}^2 \text{ s}^{-1}$, $V_w = 1.45 \text{ cm s}^{-1}$ (b) and ($L = 0.46 \text{ cm}$ $\nu = 10^{-6} \text{ m}^2 \text{ s}^{-1}$, $V_w = 1.45 \text{ cm s}^{-1}$) (c)55

Figure. 3.6 Schematic representation of the pouring mode56

Figure. 3.7 Schematic representation of the surfing mode58

Figure. 3.8 Schematic representation of ineffective surfing59

Figure. 3.9 Reynolds number calculated using u_F (Re) versus61

Figure. 3.10 Simulation snapshots of the new peristaltic wave ($\nu = 10^{-6} \text{ m}^2 \text{ s}^{-1}$ and $L = 1.11 \text{ cm}$).....63

Figure. 3.11 Front propagation in the case of $\nu = 10^{-6} \text{ m}^2 \text{ s}^{-1}$ and $L = 1.11 \text{ cm}$:...64

Figure. 3.12 Propagation of tracking particles starting in the first pocket (white) and fifth pocket (red) in the case of $v = 10^{-6} \text{ m}^2 \text{ s}^{-1}$ and $L = 1.11 \text{ cm}$: old wave (a) versus new wave (b).	65
Figure. 4.1 A photograph and microscopic images of a thrombus that has formed in a mouse after venous constriction, with platelets (αIIb) binding to deposited fibrinogen.....	70
Figure. 4.2 Illustration of the venous valve 2D geometry and particle representation.....	74
Figure. 4.3 Shear rate (a), total stress (b), pressure force (c), and velocity magnitude (d) for $L0.0256\text{m}/V0.03\text{m}\cdot\text{s}^{-1}/k_a0.01\text{J}$	81
Figure. 4.4 Snapshots taken every cycle of initial sinus fluid particles marked with color-coded displacement for $L0.0256\text{m}/V0.03\text{m}\cdot\text{s}^{-1}/k_a0.01\text{J}\sim0.05\text{J}$	83
Figure. 4.5 Velocity profile in the sinus area (vectors).	83
Figure. 4.6 Evolution of displacement (a) and peak total stress magnitude (b)...	85
Figure. 4.7 Evolution of averaged-displacement (a) and total mechanical stress (b) with the valve flexibility for simulations operated with $L0.0256\text{m}/V0.03 \text{ m}\cdot\text{s}^{-1}$	87

Figure. 4.8 Snapshots for the fluid movement of the initial sinus fluid particles marked with color-coded displacement of simulations for $L0.0256m/V0.07 m \cdot s^{-1}$ for $k_a = 0.01 J$ (a), $k_a = 0.05 J$ (b), and $k_a = 0.0001 J$	88
Figure. 4.9 Evolution of displacement (a) and total stress magnitude (b) with the maximum inlet velocity.	89
Figure. 4.10 Total stress (a), velocity magnitude (b), velocity vector (c), and displacement (d) for simulations operated with $L0.01m/V0.07m \cdot s^{-1}/k_a0.01J$	90
Figure. 4.11 Solid aggregates in the sinus region at different times for $L0.0175m/V0.07m \cdot s^{-1}/k_a0.01J$	92

LIST OF TABLES

Table 3.1 Matrix representation of the peristaltic dynamics	48
Table 3.2 Number of particles in the first 4 pockets during the first 3 haustum- periods for the pouring mode	57
Table 3.3 Matrix representation of the new peristaltic wave. The differences between the old and new wave are highlighted in bold.	63
Table 4.1 Initial parameters list for fluid and membrane	77
Table 4.2 Specific parameters adopted for models and algorithm.....	75

NOMENCLATURE

Roman letter

D	Valve chamber diameter	m
E	Elastic modulus	Pa
F	Flexural rigidity of the venous valves	N/m
Fr	Froude number	-
Ga	Galileo number	-
K	Constant for Lennard-Jones potential	J
L	Simulated intestine channel length	m
N	Pocket segment number	-
P	Agglomeration probability	-
$P_1 P_2$	Particle seeds for the agglomeration algorithm	-
P_i	Pressure of particle i	Pa
R	Relative distance between paired particles	-
T	Reciprocal of valve oscillation period	s
T_{tot}	Total mechanical stress	Pa
U_{angle}	Harmonic angle potential	N
U_{bond}	Bond potential	N
$U_{dihedral}$	Dihedral potential	N
$U_{intramolecular}$	Intramolecular potential	N
U_{tot}	Total interatomic potential	N
V	Neighbouring region volume	m ³
V_w	Velocity of peristaltic wave	cm/s
W	Smoothing kernel function	-
b	Length of pocket	cm
c	Sound speed	m/s
c_0	sound speed at zero stress	m/s
f	Oscillation frequency of valve	s ⁻¹
\mathbf{f}_i	Volumetric body force	N/m ³
g_0	Amplitude	m
h	Smoothing length	m
$i j$	Particle indices	-
k_a	Angular Hookean coefficient	J
k_b	Hookean coefficient	J/m ²
m	Mass of particle	kg
\mathbf{n}	Normal to the boundary	m
n_P	The number of tracking particles in GI tract	-
n_{TOT}	Total number of SPH particles in GI tract	-
$p_1 p_2$	Constant for Lennard-Jones potential	-

Re	Reynolds number	-
\mathbf{r}	Point location vector	m
r	Residue value	-
r_{max}	Maximum extension of the spring	m/s
r_0	Equilibrium distance of the spring	m/s
r^*	Repulsive radius of the particle	m
t	Time	s
t_w	Time interval for the intestinal wave	s
\mathbf{u}	Displacement of the solid	m
u	Initial peristaltic wave velocity	cm/s
u_F	Front velocity of peristaltic wave	cm/s
u_I	Front velocity of ineffective surfing	cm/s
u_p	Front velocity of pouring peristaltic wave	cm/s
u_S	Front velocity of surfing peristaltic wave	cm/s
\mathbf{v}_i	Velocity of particle i	m/s
x_F	Front position of peristaltic wave	cm
x_S	Front position of surfing peristaltic wave	cm

Greek Letters

Λ	geometric ratio	-
Π_{ij}	Viscous force	N
α, β	Constant parameter for artificial viscosity	-
α_d	Constant for Lucy Kernel	-
δ	Delta function	-
ϕ_{ij}	Parameter for artificial viscosity	kg·s/m ⁴
θ	The chain angle	rad
θ_0	The equilibrium angle	rad
σ_f	The stresses in the fluid	N
σ_s	The stresses in the solid	N
φ	Constant parameter for artificial viscosity	-
μ	Dynamic viscosity	N·s/m ²
ν	Kinetic viscosity	m ² /s
ρ	Density	kg/m ³
ρ_0	Density at zero stress	kg/m ³

Abbreviation

ALE	Arbitrary-Lagrangian-Eulerian
CFD	Computational fluid dynamics
CGMD	Coarse Grained Molecular Dynamics
DCM	Dynamic Colon Model
DMHS	Discrete Multi-hybrid System
DMP	Discrete multi-physics
DVT	Deep venous thrombosis
EOS	Equation of state
FSI	Fluid Structure Interaction
GI	Gastrointestinal
LB	Lattice Boltzmann
LSM	Lattice Spring Model
MD	Molecular Dynamics
MPM	Meshless Particle Method
MSM	Mass-Spring model
PE	Pulmonary Embolism
PET	Positron Emission Tomography
PIC	Particle In Cell
SPH	Smoothed Particle Hydrodynamics
VTE	Venous thromboembolism

Chapter 1 Introduction

1.1 Project Background

Computational Fluid Dynamics (CFD) is a promising tool that has been widely chosen for solving numerous engineering problems and assisting in research projects. Compared to the conventional experimental approaches, this alternative methodology takes advantage of both computer science and numeric calculation and is becoming more and more popular for its lower consumption in the virtual experimental operation together with its growing maturity and confidence in versatile practical applications. In order to yield reasonable solutions, the virtual numerical models have the naturally adaptable advantage in describing different conditions with neither costly expense of the specific materials and apparatus nor the difficulties in operating the experiments under precise constraints. What's more, the description from computational models is usually more detailed and more comprehensive since the information obtained from laboratories is often limited by the detection technology (Bradshaw, 2016). In CFD, the motion of fluids is depicted with the mathematical models developed by governing equations, which are usually in partial differential equations format. By introducing the conditions and adopting programming or software packages, the solutions for equations can be more easily to obtain with the development of analytical fluid dynamics and increase of computational power. In addition, the CFD is not only a powerful tool that can deal with various engineering problems, it can be also employed to validate the theoretical assumptions and further gains new insight into fluid dynamics (Vassberg, 2008). In

conclusion, CFD is a powerful tool aiming at the cutting edge technology and has great potential waiting for researchers to explore.

Similarly, the traditional studies for fluid dynamics inside human body are confronted with the same problems of condition controlling and the unqualified technologies for detection objectives. For example, Vogel (1996) proposed simplified stationary tissue vessel models with some fixed detection points. However, in practical experiments it is quite tricky to obtain detection devices with reasonable precision and size. Furthermore, the injury-free operation is also the essential requirement to ensure reliability of the detection results. Additionally, the tricky issue specially lies in the quantitative expression of the physiological features. Traditional researchers utilize linguistic representation that is usually intuitive owing to the subjective observations and judgements from various conditions, for instance, conventional pathologic hemodynamic reports for thrombus formation cases. Thus makes it more difficult to yield the impersonal and consistent understanding of the physiological mechanics, such as the typical pressure distribution and velocity profile of a sectional digestive tract. The system complexity can be interpreted as a combination factor that is determined by the complex structure, the detective capacity and the unpredictable movement of the biological target tissue, which further magnifies the contradiction between the traditional expression and the increasing need of quantitative description. Whether the cognition of the physiological process is accurate or not strongly depends on the correctness of the accordance of the interpretation with the facts, which is tricky to for conventional methods to give convincing criterion.

For instance, MRI image and CT scan can only give some instantaneous results. Moreover, the explanation of those results may vary from experienced doctor to inexperienced medical man owing to the judgement criteria is the summary of the clinical experience instead of the quantitative standard.

1.2 CFD applications for mathematical modelling of human physiology

Since Hermann von Helmholtz firstly introduced physics into biological components in 1845 and became the forerunner for mathematical physiology, a large number of physiologists have been utilizing the mathematical methods in understanding transport phenomena in physiological procedures (Rideout 1991, Keener and Sneyd 1998, Ebeling and Schweitzer 2002, Crosetto et al.2013).

Up to now, CFD works as the communicative bridge over the observation subjects and various numerical models; it has been developed to help the investigation into the physiological transport phenomena. Investigation into haemodynamics in cardiovascular system is one of the hottest research topics, massive noteworthy attempts have been made and fruitful progress has been achieved. For instance, a fiber-anatomically based three-dimensional model is constructed to study the blood flow inside the heart chambers with the simultaneous prediction of the motion in heart and valves (McQueen and Peskin 2000). Computational methods can also work as the only acceptable option while the experiments cannot quantitatively define the effect of the stent over the altered arteries to show the localized shear distribution and further analyze its implication in the

development of intima proliferation or restenosis (Frank et al. 2002, LaDisa et al. 2004). Some disease-specific or even patient-specific models have been introduced to reveal the correlations between the specific geometries or properties and the progression of diseases like thrombosis, aneurysms and atrial fibrillation (Wootton and Ku 1999, Sforza et al. 2009, Neal and Kerckhoffs 2009). In terms of simulations of respiratory system, virtual models are validated by experimental data and other detailed results are obtained, for instance, the particle deposition patterns (Van Ertbruggen et al. 2005), the obstruction effect over the nasal airflow characteristics (Mylavarapu et al. 2009) and the initial study of the mechanism of voice generation (Šidlof et al. 2013). Peristalsis is an important propelling mechanism for fluid transportation inside the abdominal organs. In gastrointestinal system, food content is forcedly mixed and conveyed by the periodical and peristaltic movement of the rhythmic membrane to ensure the continuous and organised advancement of food in digestive tract. Simulations have been taken and clearly demonstrate the transportation procedures and impact of some important physical properties over the dynamics (Pal et al. 2004, Akbar and Nadeem 2014, Ferrua and Singh 2015). Similar mechanism is conducted in urethra system and models are established to provide some urodynamic details to interpret the pathology, which can develop a reliable surgical reference that can help to decrease the incidence during the operation (Jin et al. 2010). CFD not only can deal with the systematic physiological problems, but also performs well in tackling smaller-scale simulations. Wurm and Zeng (2012) validate their prediction by a characteristic model of the cell disruption in nozzle and prove itself as the

first step into the simulation of cell behaviors in microfluidic geometries. The conceptual micro organ is assembled as the artificial device to demonstrate the metabolic function of liver by simulations in co-culture fashion (Schütte et al. 2011).

1.3 Project objectives

We are not aiming at the models of the complicated systems comprised of several organs in this thesis. Instead, we just focus on the local transport phenomena in some particular area. Mathematical models are built to obtain some numerical comprehension and gain some insight into the mechanism of the simulated objectives. As the physiological transport procedures usually consist of different phases, the simulation of them are considered to be the modelling of multiphase systems.

The thesis presented here has a detailed investigation into the interaction between some human elastic and deformable tissue conduits and the conveyed fluid content inside them. To be specific, the transport phenomena develops in gastrointestinal tract and deep vein valves. As Computational Fluid Dynamics has proven its reliability and proficiency in practical applications in versatile engineering fields, it can be a trustworthy tool to solve the 2D solid-liquid problems.

The gastrointestinal model are validated against the experimental results are validated against the experimental results and are built up with method coupled with Smoothed Particle Hydrodynamics (SPH) approach, which is termed as one of the most popular Lagrangian method when dealing with fluid problems. It has significant advantage over

other grid approaches owing to its mesh-free natural features when dealing with deformable boundary conditions and nonlinear wave phenomena. Additionally it can also be easily coupled with other non-grid method, such as the MSM (Mass-spring model) and CGMD(Coarse Grained Molecular Dynamics) to catch the physical characteristics of interactive segments in other phases.

As a particle method, SPH divides the investigation domain into finite number of particles instead of meshes or grids. The physical properties are carried and described by using the discrete particles. In this thesis the fluid content is represented by the SPH particle and the elastic solid boundary is modelled by other particle method. To be specific, MSM is chosen for the venous valves and CGMD is chosen for the gastrointestinal tract. By this way we take the most advantage of the coupled methods, which makes the models much easier to construct and closer to the real biological states and thus to yield more realistic and accurate results. Combine the mesh-free nature of SPH with the advantage of the MSM/CGMD method, the couple method gains the new ability of flexible treatment of soft boundaries. The coupled methodology is termed as Discrete Multi-hybrid System (DMHS) collectively and has been validated in many multiphase systems, it can refer to as Coarse Grained Molecular Dynamics (CGMD) or Mass-Spring model (MSM) in view of the scale difference.

1.4 Thesis Layout

Firstly a thorough theoretical background is given to show the general process routine in the simulations completed by SPH method only in Literature Review chapter. The basic application of SPH method is presented here with classical cases implemented by codes written in C++ language and the results are validated against the analytical solutions.

Then the following chapter III focused on the two-phase system built up with DMHS hybrid method. A brief introduction is given first to show the coupling models for solid-liquid system. To validate the models proposed ahead, an adjustment is made to mimic the flows propelled by a section of colon muscle. Quantitative comparisons are made among the fluid viscosities ranging from relative fluidity to high viscosity with regard to real fluids in colon, various muscle propelling speed and different peristaltic modes to show how the food is mixed, transported with periodic peristaltic systems. The results are compared with the experimental outcome from Positron Emission Computed Tomography (PET) system, which shows good agreement with our data.

In addition, this coupled hybrid method is also adopted in the venous flow system and shows its great adaptability in different systems in chapter IV. Comparisons are made of flows under various periodic external force conditions goes through valves with different lengths and various flexibilities. Results show how the pulsatile blood flows develops and its transportation in the valvular deep veins. The phenomena due to the dysfunction of valves are clearly showed and analyzed, which can be a good start of the pathological learning of the deep veins thrombosis by CFD approach.

Finally a conclusion chapter V is given to make the summary of the completed work and outcome, analysis of the results, the discussion and suggestion of the future work.

The study consists of two publications:

1. Alexiadis, A., Stamatopoulos, K., Wen, W., Batchelor, H. K., Bakalis, S., Barigou, M., Simmons, M. J. H. (2017). Using discrete multi-physics for detailed exploration of hydrodynamics in an in vitro colon system. *Computers in biology and medicine*, 81, 188-198. (Chapter II and Chapter III)
2. Ariane, M., Wen, W., Vigolo, D., Brill, A., Nash, F. G. B., Barigou, M., Alexiadis, A. (2017). Modelling and simulation of flow and agglomeration in deep veins valves using discrete multi physics. *Computers in biology and medicine*, 89, 96-103. (Chapter IV)

Chapter 2 Literature Review

2.1 Introduction

With the increasing of the computational power and the advancement of the simulation techniques, the Computational Fluid Dynamics (CFD) is becoming more and more applicable and popular in practical fields. Hence, it is possible that the approximate solutions for differential governing equations in fluid dynamics can be obtained by versatile numerical methods. It is widely known that those governing equations can be interpreted by either Lagrangian or Eulerian way. These descriptions differ from the choice of the frame of coordinates; those who belong to Eulerian approaches fix their coordinates on the spatial nodes and preserve their locations when time elapses. While the others in Lagrangian type are built up on the material points and they keep their position in consonance with the material during the development of the flow. Their discrepancy in coordinate system is recognized as the fundamental distinction and is used as the most popular reference to make the classifications.

SPH is a pure Lagrangian method and was one of the earliest meshless methods proposed about four decades ago by Lucy (1977), meanwhile Gingold and Monaghan (1977) independently. It sets a pioneering example for the development of the Meshless Particle Method (MPM) when firstly adopted in the investigation of the astronomical problems.

After approximate forty years of development, SPH is now approaching its mature stage and its applications range from the cosmological phenomena to the microscale interaction,

prove itself a practical technique for versatile engineering problems. Various applications have been applied into astronomy (Springel and Hernquist 2003, Stinson et al. 2010, Springel 2011, Nelson et al. 2013), coastal hydrodynamics (Monaghan and Kos 1999, Krištof et al. 2009, Altomare et al. 2015), conduction (Clearly and Monaghan 1999), explosion and collisions (Liu et al. 2003, Aguiar et al. 2001), metal forming and die casting (Bonet and Kulasegaram 2000), controlling system for vehicles or robots (Lipinski and Mohseni 2010, Pimenta et al. 2013), solid cracking and earthquake (Benz and Asphaug 1995, Huang et al. 2012), circulatory system (Shahriari et al. 2012), etc. It is widely witnessed that SPH has the giant power in solving problems from diverse fields and its great potential is trustworthy that it can develop itself into the novel approach for more extensive applications.

As mentioned above, SPH method does not employ stationary mesh or invariant grid as the auxiliary tool for the simulation and the problem domain is purely represented by a certain group of discrete particles. In other word, the particle in SPH method not only has the realistic material identity that carries various physical properties with it, but is also integrated with the mathematical function and works as the interpolation point to yield the solutions of the governing equations. For instance, while a typical particle method called Particle In Cell (PIC) (Birdsall, 1991) employs grids for the derivative calculation of variables, SPH updates the value of field variables and their derivatives for each particle directly with weighted integral approximation of those from the neighbouring particles at every time step and the results are not affected by the distribution arbitrariness

of neighbouring particles. In this way it combines the continuum of materials and the discretization of target domain together naturally. To this extent, the computational power for the advection term when dealing with equations of fluid dynamics is also reduced accordingly. This is one attractive feature for SPH that it has the inherent advantage in treating advection since it can directly track the historical trajectory of the particles and hence the development of the material segment can be easily observed. This makes contributions to SPH to have a special adaptive feature when confronted with problems involving complex geometries, free surface, large deformation, deep penetration or strong discontinuity. Similarly, SPH also stands out for the interfacial treatment. It can easily approximate the interface by defining multiple materials with different particle groups without adding extra massive pre-treatment, which is quite tricky for grid methods when there exists large deformation or irregularity of interfaces. Besides, as the particle in SPH possesses volume and mass which acts as the finite unit of the materials, from this feature it has the similar character to another type of simulation approach called Molecular Dynamics (MD) method. The analogy to MD method makes it communicative and feasible to be integrated into coupled methods, therefore by which the resolution of both methods can be extended. In this way the SPH method can be coupled with CGMD/MSM method to share the integrated advantages. The coupling methods are available for multiscale problems and thus show their abilities in various applications especially for biological flows incorporate deformable and multi-size items (Cleary et al. 2013).

Though it is not a commonly used approach to establish the biological models, SPH has great potential to become a superior tool for biological applications. In blood flows, it can be used to predict the flow patterns of the viscous blood within a straight vessel and reaches a good agreement with the experimental results (Al-Saad 2007). It can simulate the impenetrable biological membranes and reproduce the classic physical experiments (Palyanov et al. 2016). It is also suitable for modelling irregular shaped bones and can be easily adopted in solving complex geometries (Topalović et al. 2015).

This chapter provides the basic concept and the essential formulation of SPH method, a brief routine is given sequentially to illustrate the general procedure of conducted simulation. The validation of method is accomplished by results against the analytical solutions for some benchmark examples, which can be considered as the basic foundation for further extensive implementation of the algorithm coupled with other mesh-free methods.

2.2 Basic SPH concept

2.2.1 Integral approximation

At the moment, the main purpose for numerical fluid simulations is to utilize a felicitous algorithm to get reasonable approximate solutions for governing equations while the accurate analytical solutions or the experimental results are neither accessible nor economical. In SPH these equations usually can be transformed from partial differential equations into ordinary differential equations and can be approximately solved by

weighted integration over interactive neighbouring particles, which are identified by their physical properties, such as the mass and the density, the velocity and the pressure.

The fundamental idea behind this discrete approximation lies in the mathematical identity

$$f(\mathbf{r}) = \iiint f(\mathbf{r}')\delta(\mathbf{r} - \mathbf{r}')\mathbf{d}\mathbf{r}', \quad (2.1)$$

where $f(\mathbf{r})$ is a generic function defined over the volume V , the vector \mathbf{r} is a three-dimensional point in V and $\delta(\mathbf{r})$ is the three-dimensional delta function. This integral representation is termed as the foundational preparation step for constructing SPH concept.

In the SPH formalism, the delta function is approximated by a function W called the smoothing kernel with a characteristic width h (smoothing length) such that

$$\lim_{h \rightarrow 0} W(\mathbf{r}, h) = \delta(\mathbf{r}). \quad (2.2)$$

This brings the approximation

$$f(\mathbf{r}) \approx \iiint f(\mathbf{r}')W(\mathbf{r} - \mathbf{r}', h)\mathbf{d}\mathbf{r}', \quad (2.3)$$

In addition, the kernel function is usually a function symmetrically divided by position difference with respect to point \mathbf{r} with the effective compact volume, and its integration over the volume is equal to unity. If the supported domain is not compact, actions can be taken for the compensation and the classic example will be shown in the following section.

By replacing $f(\mathbf{r}')$ with its Taylor series expansions it is not difficult to infer that the kernel function has the accuracy of second order

$$\begin{aligned}
f(\mathbf{r}) &\approx \iiint [f(\mathbf{r}) + f'(\mathbf{r}' - \mathbf{r}) + r((\mathbf{r}' - \mathbf{r})^2)]W(\mathbf{r} - \mathbf{r}', h)\mathbf{d}\mathbf{r}' \\
&= f(\mathbf{r}) \iiint W(\mathbf{r} - \mathbf{r}', h)\mathbf{d}\mathbf{r}' + f'(\mathbf{r}) \iiint (\mathbf{r}' - \mathbf{r})W(\mathbf{r} - \mathbf{r}', h)\mathbf{d}\mathbf{r}' + r(h^2) \\
&= f(\mathbf{r}) + r(h^2).
\end{aligned} \tag{2.4}$$

Equation 2.4 just shows how to obtain the accuracy for kernel functions used in SPH method, more detailed information of smoothing kernel is further introduced in the following part of this chapter.

Likewise, the derivatives of properties can be yielded in the similar way. In other word, the derivative operation on field function is transformed into the derivative of the kernel function like this

$$\begin{aligned}
\nabla \cdot f(\mathbf{r}) &\approx \iiint [\nabla \cdot f(\mathbf{r}')]W(\mathbf{r} - \mathbf{r}', h)\mathbf{d}\mathbf{r}' \\
&= \iiint \nabla \cdot [f(\mathbf{r}')W(\mathbf{r} - \mathbf{r}', h)]\mathbf{d}\mathbf{r}' - \iiint f(\mathbf{r}')\nabla W(\mathbf{r} - \mathbf{r}', h)\mathbf{d}\mathbf{r}' \\
&= - \iiint f(\mathbf{r}')\nabla W(\mathbf{r} - \mathbf{r}', h)\mathbf{d}\mathbf{r}'
\end{aligned} \tag{2.5}$$

Generally speaking the first step of SPH formulation is completed by the approximate operations of smoothing kernel. Therefore the target approximate values can be mathematically simplified into the corresponding derivative operations over kernel function.

2.2.2 Particle approximation

Kernel functions are used for the mathematical approximation, but the closure of SPH formulation still needs the link between the physical estimate and the particle representation, which is achieved by the particle approximation.

Equation 2.5 can be discretised over a series of particles of mass $m = \rho(\mathbf{r})d\mathbf{r}$ obtaining

$$f(\mathbf{r}) \approx \sum_i \frac{m_i}{\rho_i} f(\mathbf{r}_i) W(\mathbf{r} - \mathbf{r}_i, h), \quad (2.6)$$

where $f(\mathbf{r}_i)$, m_i and ρ_i are the mass and density of the i^{th} particle, and i ranges over all particles within the smoothing kernel radius. This is a pivotal step that transfers the continuous integral representation into the summation over a defined group of scattered particles with the introduction of vital properties like mass and density.

Similarity lies in the presentation of derivative of functions. Combine Equation 2.6 and Equation 2.5 it can reach a conclusion that

$$\nabla \cdot f(\mathbf{r}_i) \approx \sum_j \frac{m_j}{\rho_j} f(\mathbf{r}_j) \cdot \nabla_i W_{ij}, \quad (2.7)$$

where $W_{i,j}$ means $W(\mathbf{r}_j - \mathbf{r}_i, h)$, j denotes the neighbouring particle within the compact domain and ∇_i denotes the gradient of the kernel with respect of the coordinate r_i .

The SPH approximation is completed by the two-step integral approximation (Equation 2.6 and 2.7) without pre-defined grids and particles work as flexible nodes that also carry physical identities with them, whose distribution sets the resolution for the computational frame in the upcoming simulations.

2.2.3 Kernel function

Kernel function plays as a decisive factor in the computational results over the simulation domain. The choice of smoothing kernel not only indicates the distinct approximation fashion, the support domain is self-defined owing to the of the function characteristic, but also has influence on the accuracy of the obtained solutions.

Some properties of smoothing kernel have been stated in section 2.2.1 like the unity, symmetric, compact support and delta function resemblance. Sometimes further specific adjustments are added to compose the reasonable functions, for instance, the physical phenomena with discontinuities can be solved by the boundary treatment, which will be explained by examples in the following chapter.

To conserve the physical connotation of the discrete particles, the value of the kernel function should be non-negative to eliminate the unrealistic error like the negative mass or energy and continuously ensure that all the physical properties of the corresponding particles are meaningful during the whole simulation. Besides, as a function acts on the limited area, the interaction between particles from shorter distance should be stronger than those particles from more distant areas. Mathematically speaking, the function should be monotonically decrease with the increase of the distance between neighbouring particles, which is consistent with its compact property. What's more, as it is termed as the smoothing kernel, it should have sufficient smoothness that can adequately reduce the detrimental effect from the irregular particle distribution, smooth out the fluctuations in the calculation by the weighted integral representation, and therefore help to get more

accurate approximation. Only under these constraints that a function can be possibly considered as an alternative smoothing kernel, and after years of development many of them have been adopted in the practice. Here some widely used functions will be briefly introduced in the following section.

Lucy's kernel is the oldest smoothing function and was first adopted in astronomical investigation (Lucy 1977). This bell-shaped function is easy to implement in constructing SPH models and can be adapted for diversified multidimensional problems.

$$W(R, h) = \alpha_d \begin{cases} (1 + 3R)(1 - R)^3 & R \leq 1 \\ 0 & R > 1 \end{cases} \quad (2.8)$$

where R stands for the relative distance between neighbouring pair particles with comparison to smoothing length h , and α_d ranges from $5/4h$, $5/\pi h^2$, $105/16\pi h^3$ for one-, two- and three-dimensional space, respectively. In this function the support domain is constrained with the radius equal to the predefined smoothing length.

Monaghan (1992) strongly suggested that the best choice for smoothing kernel is in Gaussian pattern for physical interpretation of an equation in SPH style. Up to now the most extensively used one, namely, cubic B-spline function, is proposed by Monaghan and Lattanzio (1985) due to its performing as an analogy to the Gaussian function with a more compact support domain. However the piecewise fashion of function makes it more complex in implementation for practical usage and less stable compared to one-piece kernels.

$$W(R, h) = \alpha_d \begin{cases} \frac{2}{3} - R^2 + \frac{1}{2}R^3 & 0 \leq R < 1 \\ \frac{1}{6}(2 - R)^2 & 1 \leq R < 2 \\ 0 & R \geq 2 \end{cases} \quad (2.9)$$

2.3 Governing equations

The above section introduces the basic formulation procedure of SPH combining both the numerical aspects and physical features together with the essential mathematical approximation tools called smoothing kernel performed as the transformer between both aspects.

In this subsection the applications of SPH method in fluid dynamics will be briefly introduced. To conclude, all the development of fluids are under the constraints of the conservation laws which can be expressed by some governing equations, such as the momentum equation or the continuity equation. The equations can be represented in either Lagrangian or Eulerian description based on different criteria. Due to the purely Lagrangian feature of SPH method, these equations are in only Lagrangian fashion under SPH description.

An assumption is made that all the simulation procedures in this thesis are taken under the isothermal system, which naturally do not take the thermodynamics into the considerations. So the discussion about conservation of energy is not included in this thesis.

2.3.1 The momentum equation

Equation (2.10) represents the discrete approximation of a general continuous field and can be used to approximate the Navier-Stokes equation

$$\frac{d\mathbf{v}_i}{dt} = \sum_j m_j \left(\frac{P_i}{\rho_i^2} + \frac{P_j}{\rho_j^2} + \Pi_{i,j} \right) \nabla_j W_{i,j} + \mathbf{f}_i, \quad (2.10)$$

where \mathbf{v}_i is the velocity of particle i , P_i is the pressure, \mathbf{f}_i a volumetric body force, and $\Pi_{i,j}$ introduces the viscous forces. At each time step, equation (2.10) is used to update the velocities of the fluid particle. Mathematically speaking, the spatial differential equations are replaced by the ordinary differential equations only with time (equation (2.5) and (2.7)), this reasonable approximation sufficiently decreases the computational complexity and saves the calculation power. In early SPH models the viscous tensor is usually not included as the corresponding Euler equations do not take viscosity into consideration. Up to now various expressions for the tensor $\Pi_{i,j}$ are available in the literature. A detailed discussion is provided in the following section 2.3.3 of this chapter.

The equation of motion of the SPH particles follows from equation (2.10):

$$m_i \frac{d^2 \mathbf{r}_i}{dt^2} = \sum_j m_i m_j \left(\frac{P_i}{\rho_i^2} + \frac{P_j}{\rho_j^2} + \Pi_{i,j} \right) \nabla_j W_{i,j} + \mathbf{f}_i. \quad (2.11)$$

In order to close equation (2.11), calculation for density and an equation of state linking ρ and P is required. Both of them are discussed in 2.3.4 in details of this chapter.

2.3.2 The continuity equation

Continuity equation is usually regarded as a stronger and local form for the conservation law. In SPH, the continuity equation can be interpreted in several ways and therefore expressed in different format.

Generally speaking, the density can be calculated either by equation (2.6), considering ρ as a normal scalar field yielded by integration over its supporting domain, which is the simplest alternative called summation density, taking the direct usage of integral representation of function for every particle,

$$\rho_j \approx \sum_i m_i W(\mathbf{r} - \mathbf{r}_i, h), \quad (2.12)$$

or another choice termed as continuity density, obtaining the density indirectly from its variation with respect to time by means of the discrete approximation of the differential continuity equation,

$$\frac{d\rho_i}{dt} = \sum_j m_j \mathbf{v}_{i,j} \nabla_j W_{i,j}, \quad (2.13)$$

where $\mathbf{v}_{i,j} = \mathbf{v}_i - \mathbf{v}_j$. This equation reveals the relationship between velocity difference and the density change rate with time, and the proportion is determined by the gradient of the chosen kernel function.

Either integral or differential implementation of continuity equation in SPH style is widely adopted. The summation approach preserves the SPH feature well and conserves the mass inherently, but it also has the edge deficiency when confronting with boundaries or material interfaces. The accuracy of particles under these conditions is likely to suffer

from the insufficient support domain owing to the boundary truncation, the lack of neighbouring particles or the multi-material density discontinuity. Available proper boundary treatments and some modifications to the algorithm like normalization can be selected to remedy the deficiency. However the computational burden of modified method is further increased since the original approach has already required a relative huge computational consumption due to the prior calculation order for density. Therefore in the case of the general flows the summation density seems more popular for its simple implementation and its good representation of SPH nature. When there exists discontinuity phenomena like explosion or shocks, the continuity density is more welcome to reduce the errors coming from the density discontinuity or particle deficiency, which is effectively achieved by the employment of the absolute relative velocity. Besides, the computation effort is also saved owing to its flexible calculation scheme whose order do not follow a requisite sequence to calculate the density before other properties.

The choice between two widely accepted approaches is based upon the concrete requirements from diversified specific conditions, and what's more, special treatment and modifications can be also added to modify the original algorithm if needed.

2.3.3 The viscous term

In the early implementation of SPH, the viscosity is not included in the Euler equations that used to represent the conservation laws. Most applications are limited into the inviscid problems owing to its instable and inaccurate expression for the second-order spatial velocity derivative term for the viscous force calculation. Typical examples shown

in some investigations discretised into low resolution with low-order kernels adopted are easily prone to suffer from instability (Sigalotti et al. 2003, Yang et al. 2014). But with regard to the Navier-Stokes equations in SPH format, there are various implementations of viscosity models, which are usually case-basely selected to yield precise simulation results.

Apart from the realistic viscosity, artificial viscosity models in SPH can play additional function that helps to remedy the numerical error and regularize the instability with artificial modifications, which is commonly adopted in the investigation of shock waves (Monaghan and Gingold 1983, Agertz et al. 2007, Ren et al. 2015) to reduce the excessive oscillation and obtain reasonable physical discontinuity; or high velocity impact to handle severe distortions (Johnson et al. 1996).The most popular and frequently used model is the standard artificial viscosity given by Monaghan(1992) as the extension of von Newman-Ritchter type proposed for shock simulations (Von Neumann and Richtmyer 1950)

$$\Pi_{i,j} = \begin{cases} \frac{-\alpha \bar{c}_{ij} \phi_{ij} + \beta \phi_{ij}^2}{\bar{\rho}_{ij}} & \mathbf{v}_{ij} \cdot \mathbf{x}_{ij} < 0 \\ 0 & \mathbf{v}_{ij} \cdot \mathbf{x}_{ij} \geq 0 \end{cases} \quad (2.14)$$

where

$$\phi_{ij} = \frac{h_{ij} \mathbf{v}_{ij} \cdot \mathbf{x}_{ij}}{|\mathbf{x}_{ij}|^2 + \varphi^2} \quad (2.15)$$

$$\bar{c}_{ij} = \frac{1}{2} (c_i + c_j) \quad (2.16)$$

$$\bar{\rho}_{ij} = \frac{1}{2} (\rho_i + \rho_j) \quad (2.17)$$

$$h_{ij} = \frac{1}{2}(h_i + h_j) \quad (2.18)$$

$$\mathbf{v}_{ij} = \mathbf{v}_i - \mathbf{v}_j, \mathbf{x}_{ij} = \mathbf{x}_i - \mathbf{x}_j \quad (2.19)$$

and α, β are constant parameters whose values are usually chosen around 1, $\varphi = 0.1h_{ij}$ is adopted to avoid numerical divergence. The first linear term in the artificial viscosity associated with α produces the bulk viscosity. The shear viscosity is represented by the second quadratic term resembles von Newman-Richtler viscosity that helps to prevent the particle penetration and eliminate the singularity when the particle distance is too close. The values of α and β can alter according to the specific requirements from a variety of cases. This symmetric form of artificial viscosity guarantees both the linear momentum and the angular momentum conservation, which plays a vital role in solving the problems involved with high velocity or sharp front. Up to now diverse extension and modification have been made to further extend the applications for various artificial viscosity models. For instance, in some investigations for astrophysical problems such as accretion discs and galaxy clusters, the second quadratic term is often excluded to avoid the extra-large viscosity and then the so-called nested summation approximation concerning physical viscosity (Riffert and Herold 1995) is included to introduce the viscous force to produce better disc approximation and capture substantial turbulent gas motions (Lanzafame 2003, Dolag et al. 2005). In regard to high viscosity industrial issues, it also shows great adaptiveness and can be easily coupled with other mesh-free method for more complex problems (Peer et al. 2015).

Here we use the Morris' formulation (Morris et al. 1997) for low Reynolds numbers, which is suitable for low velocity incompressible flows, and the momentum equation can be described as below

$$\frac{D\mathbf{v}_i^\alpha}{Dt} = - \sum_{j=1}^N m_j \left(\frac{p_i}{\rho_i^2} + \frac{p_j}{\rho_j^2} \right) \frac{\partial W_{ij}}{\partial x_i^\alpha} + \sum_{j=1}^N m_j \left(\frac{\mu_i + \mu_j}{\rho_i \rho_j} \right) \mathbf{v}_{ij}^\beta \left(\frac{1}{r_{ij}} \frac{\partial W_{ij}}{\partial r_{ij}} \right) \quad (2.20)$$

Where μ denotes the dynamic fluid viscosity, choice of α and β is based on the practical requirements.

2.3.4 Equation of state and artificial compressibility

The lengthy description of the common equation of state (EOS) adopted for incompressible flow results in an unpractical time increment. Therefore the excess shortness in time step will lead to extremely high computational load even though calculations can be slightly more efficient by introducing a fixed density. What's more, it is not practical to simulate a perfectly incompressible flow and therefore an assumption can be made that the flow can be regarded as slightly compressible. In this way we can employ the artificial viscosity in the compressible EOS to better approximate the real state. Therefore the time derivative of the pressure is produced by introduction of the artificial viscosity. For simulations of single phase incompressible flow with low Reynolds number, this style of EOS can be a good option (Tamamidis et al. 1996)

$$p = c^2 \rho \quad (2.21)$$

where c is the sound speed and a smaller scale is chosen here to create an artificial compressibility. Choice of its values is based on the compromise of the practical

compressibility and the time interval. Additionally the estimated pressure can also assist to determine the proper value (Morris et al. 1997).

Another alternative like Tait's equation of state (Batchelor and Young 1968) can be also applied to water to determine the pressure, here the incomplete style is used, that is to say, only the liquid density is taken into consideration without the temperature issue to simply the computation.

$$P(\rho) = \frac{c_0 \rho_0}{7} \left[\left(\frac{\rho}{\rho_0} \right)^7 - 1 \right] \quad (2.22)$$

where c_0 and ρ_0 are, respectively, the sound speed and density at zero stress.

Both the obtained outcome can be added directly as the pressure term and results obtained from the artificial compressibility assumption have been confirmed to agree well with precious studies especially for applications for certain theoretically incompressible flows concerning free surface (Monaghan 1994, Becker and Teschner 2007, Ferrari 2010).

2.4 Boundary treatment

The boundary conditions for free surfaces are spontaneously satisfied in SPH method owing to its mesh-free character together with the governing equations in Lagrangian format. However when it is adopted for the solid boundaries, it is prone to lead to a truncated support domain for the particles nearby. Insufficiency in number of neighbouring particles will lower the accuracy in relevant calculations, for instance, the updated gradient for the velocity computation. The boundary conditions can be amended in certain ways. The most broadly used option for the boundary treatment is to virtually

generate artificial particles near or/and on the boundaries with repulsion to the real particles, creating an impermeable environment that stops the particles from seeping through the cracks (Morris et al. 1997).

2.5 Coarse-Grained Molecular Dynamics (CGMD) / Mass-spring modelling

(MSM)

Molecular dynamics is a form of investigation where the motion and the interaction of a certain number of computational atoms or molecules are studied. In classical MD simulations atoms move according to the Newtonian equations of motion

$$m_i \frac{d^2 r_i}{dt^2} = - \frac{\partial}{\partial r} U_{tot}(r_1, r_2, \dots, r_N), \quad (2.23)$$

where U_{tot} is the total interatomic potential, which can be divided into two main parts: non bonded and intramolecular. Non bonded forces are usually represented by the so-called Lennard-Jones potential, while the intramolecular forces are often divided in subgroups

$$U_{intramolecular} = U_{bond} + U_{angle} + U_{dihedral} \quad (2.24)$$

Each of these potentials can adopt different forms. In this study, the dihedral potential is not used, and the non-linear bond potential is used

$$U_{bond} = \frac{k_b (r - r_0)^2}{[r_{max}^2 - (r - r_0)^2]} \quad (2.25)$$

where k_b a Hookean coefficient, r_0 the equilibrium distance, and r_{max} the maximum extension of the spring, and the harmonic angle potential

$$U_{angle} = k_a(\theta - \theta_0)^2 \quad (2.26)$$

where k_a is an angular Hookean coefficient and θ_0 the equilibrium angle,

Equations (2.23—2.26) are the basis for the ball-and-stick representation of molecules that can be termed as coarse-grained to model macroscopic solids. The detailed structure is shown in the following two chapters. This approach can be employed to model macroscopic phenomena such as stretching and bending of solids under the effect of external forces. In the case under investigation, the macroscopic membrane is divided into a certain number of notional particles and use the potentials of Eq. (2.25) and Eq.(2.26) to simulate its deformation. How bond and angle potentials are used will be shown in next chapter by intestine model presented below and venous valve model. This component of the DMHS has been indicated sometimes as CGMD and sometimes as MSM. The mathematical formulation is the same: at small scales (e.g. microfluidic applications) the term CGMD is preferred (e.g. Alexiadis 2015), at larger scales the term MSM (e.g. Ariane 2017) is preferred.

2.6 Coupling the two models/ discrete multi-hybrid system (DMHS)

The interaction between the solid (CGMD particles) and the liquid (SPH particles) is defined by boundary conditions, which relate the behaviour of two adjacent materials at the common interface. There are three main types of phenomena that must be taken into consideration in designing these boundary conditions (Müller et al. 2004): no-penetration,

no-slip and continuity of stresses. In continuum mechanics, these conditions are often represented as

$$\left(\frac{\partial}{\partial t} \mathbf{u} - \mathbf{v}\right) \cdot \mathbf{n} = 0 \text{ (no - penetration),} \quad (2.27)$$

$$\left(\frac{\partial}{\partial t} \mathbf{u} - \mathbf{v}\right) \times \mathbf{n} = 0 \text{ (no - slip)} \quad (2.28)$$

$$\sigma_s \mathbf{n} = \sigma_f (-\mathbf{n}) \text{ (continuity of stresses)} \quad (2.29)$$

where \mathbf{n} is the normal to the boundary, \mathbf{u} the displacement of the solid, \mathbf{v} the velocity of the liquid, σ_s the stresses in the solid and σ_f in the fluid.

In the particle framework, the no-penetration conditions is often implemented by means of an additional central force with a Lennard-Jones form

$$f(r) = K \left[\left(\frac{r^*}{r}\right)^{p_1} - \left(\frac{r^*}{r}\right)^{p_2} \right] \frac{\mathbf{r}}{r^2} \quad (2.30)$$

where r^* represents the repulsive radius of the particle, and p_1 and p_2 are usually set to 4 and 2, and sometimes the original 12-6 Lennard-Jones values are selected. The constant K has the unit of V^2 and is often chosen on the basis of a characteristic velocity of the flow. The no-slip condition models the friction between the solid and the fluid. In finite-element numerical methods it is often enforced by imposing that the two materials have the same velocity at the interface. In our SPH-CGMD framework, a similar strategy can be achieved by superimposing a fluid ghost particle above the solid particles at the interface and examples are given in the following chapters. The advantage of using a particle-particle representation is that, once both the no-penetration and no-slip boundary

condition are enforced, the continuity of stress is automatically satisfied by the equation of motion (2.11). And this type of coupling is termed as discrete multi-hybrid system (DMHS) by Alexiadis (2015a).

2.7 Benchmark verification

This section will display two classical numerical tests to validate the model built on SPH theory. The model is implemented by codes and a simplified description of the essential steps in the simulation routines is given below. They can be treated as a good start-up of the following simulations utilizing the coupled CGMD method.

2.7.1 The basic structure of the simulation

Here a simple flow chart of the implementation of hybrid particle type method is provided, similarly, the upcoming introductory tests also follow the common flow chart. The simulation indeed starts with the establishment of geometrical treatment according to the initialization information of physical circumstances. Different types of employed particles confined by constraints are attuned to the practical requirements of simulation for the reasonable approximation of the realistic conditions. After the completion of the initialization of problem domain, the data index can be generated by serial numbering and all the information is stored in the linked list for the convenience of fast traversal, so the usage of neighbouring lists becomes more convenient. So far the preparation is completely done by the systematic initialization built from the SPH method. The calculation of interior and exterior forces generates overall acceleration for each particle,

the particle information is updated by Velocity-Verlet scheme (Verlet 1967) and the data index is also updated every single time step. Up until the counting number of time step reaches its end, a detailed time trajectory is continuously renewed by the historical record, which is a specific strength supported by particle style method. This integration is the most essential and affecting step that determines the accuracy of the outcome and different characterized treatments are adopted for diverse requirements. In this chapter some classic examples will be presented below.

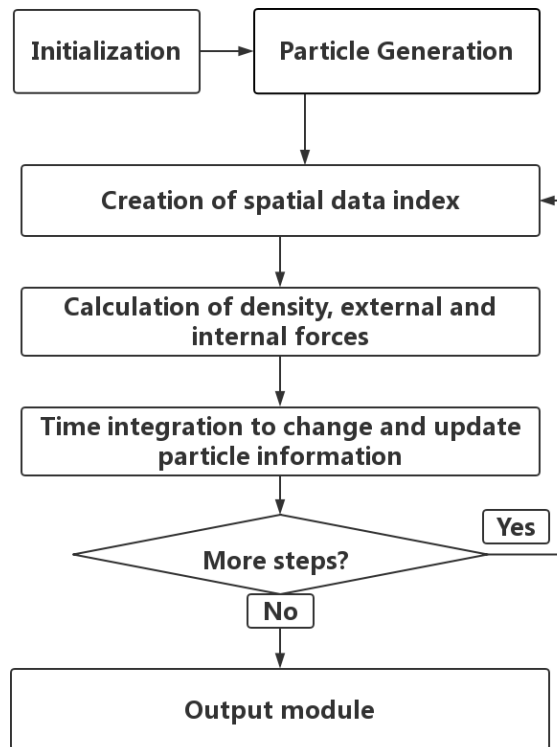


Figure. 2.1 Standard solution process for coupled molecular method

2.7.2 General description of two cases

Here the essential background information will be outlined for the case problems called Poiseuille flow and Couette flow. Both of them are theoretically incompressible flow and reach to their steady state finally.

The Poiseuille flow we study here is an incompressible flow driven from static state by a steady body force $F = 2 \cdot 10^{-4} m/s^2$ and gradually develops between two parallel infinite planes perpendicular to the body force and fixed still on $y = -l/2$ and $y = l/2$, where $l = 10^{-3} m$.

For the limitations mentioned above, the issue of getting the solution of instantaneous velocity profile can be easily simplified by complexity reduction by means of dimension descending. This is owing to the constrained flow direction by the unidirectional and steady body force. Moreover the calculation is further simplified owing to the constant viscosity character of the working fluid, therefore here the equation (2.10) is used and equation (2.13) in one dimension format to provide the solution, that is

$$V_x(y) = -\frac{F}{2\nu} \left(\frac{l^2}{4} - y^2 \right) \quad (2.31)$$

where the kinetic viscosity is an invariant that $\nu = 10^{-6} m^2/s$, and the highest speed value of the fluid is $V_p = 2.5 \cdot 10^{-5} m/s$, thus the flow is a typical laminar flow with its $Re = \frac{V_p l}{\nu} = 2.5 \cdot 10^{-2}$.

The instantaneous velocities for all particles can be obtained via this theoretical solution (Morris et al. 1997):

$$\begin{aligned}
V_x(y, t) = & \frac{F}{2\nu} y(y - l) \\
& + \sum_{n=0}^{\infty} \frac{4Fl^2}{\nu\pi^3(2n+1)^3} \sin\left(\frac{\pi y}{l}(2n+1)\right) \exp\left(-\frac{(2n+1)^2\pi^2\nu}{l^2}t\right)
\end{aligned} \tag{2.32}$$

Similarly, the Couette flow is also a laminar flow which shares the same the initial state and Reynolds number as Poisuille flow. Then the flow is generated immediately by the upper plane advances with an invariable velocity $V_u = 2.5 \cdot 10^{-5}m/s$ during the whole simulation.

Analogously the analytical solution for Couette flow is given as (Morris et al. 1997):

$$V_x(y, t) = \frac{V_u}{l} y + \sum_{n=1}^{\infty} \frac{2V_u}{n\pi} (-1)^n \sin\left(\frac{n\pi y}{l}\right) \exp\left(-\frac{n^2\pi^2\nu}{l^2}t\right) \tag{2.32}$$

2.7.2 The specific treatment of the simulations

As the simulations in this subsection are purely implemented by SPH method, treatments only related to SPH particle method are depicted below.

As for the initialization procedure, theoretically the two parallel planes should be infinite long to unceasingly maintain the internal flow character. Since this goal is unreal to achieve for the geometric treatment, then a compromise is made on the boundary treatment to meet the same requirement: when the flow goes out from the outlet it directly goes back into the inlet, therefore an equivalent transformation can be made that the flows are constrained by the closed boundary of the cylindrical curved surface.

Additionally in this way the computation load is reduced. For easier comparison with the analytical results, the geometrical treatment is set as rectangle type, $5 \cdot 10^{-4}m$ in length for x direction and $10^{-3}m$ in width for y direction, and particles in same group are placed evenly as well. As it is shown below in Figure 2.2, the flow is restricted in the computational region by means of two parallel boundary edges represented by 40×2 dummy particles. As for the working fluid domain, it is filled with 40×80 real particles. The time step is chosen as 0.0001s and after about 5000 steps the flow obtains its steady state. From the specific boundary treatment, an assumption can be made that there exists an evolving wraparound effect during the developing stage of the flow, that is the phenomenon occurs when the initial upstream go directly back to the inlet after it flows out of the outlet, and thus as if it became the downstream of the original downstream part, forming a gradually developing curve owing to the cylindrical periodic boundary treatment. For easier comparisons, same time step is used for each flow. As Figure 2.3 shows, an obvious wrapping up of the flow front from the flow tail supported the hypothesis in this instantaneous profile of the fluid particle location.

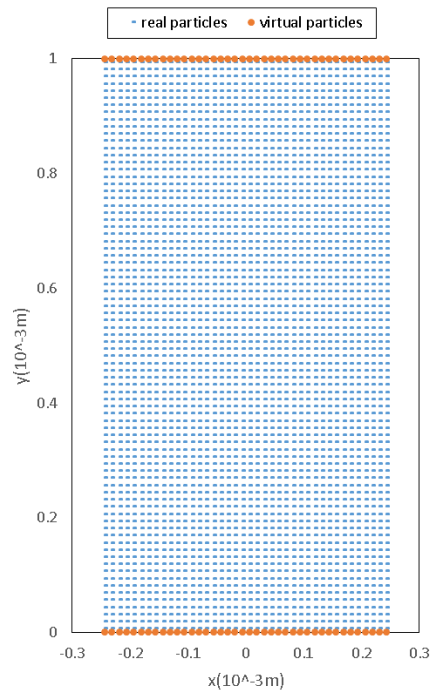


Figure. 2.2 Initial geometrical treatment for the simulation of Poiseuille flow and Couette flow

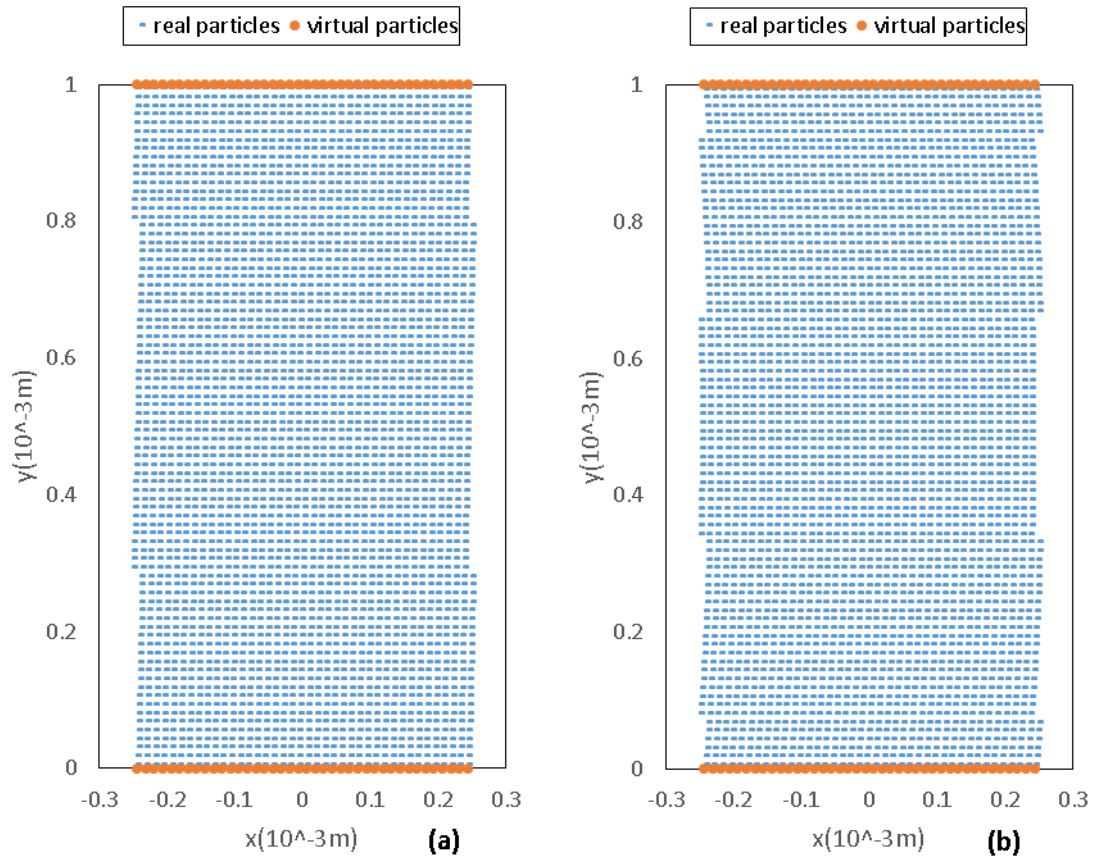


Figure. 2.3 Fluid particle distribution for (a) Couette flow and (b) Poiseuille flow at $t=1s$

2.7.3 Validation against theoretical solutions

Results from the SPH method are validated by the comparison with the analytical outcome. The method outcome agree well with the serial solutions at three time steps, two at the development stage while the last one for the steady state, namely, $t=0.01s$, $0.1s$, $t=1s$. This plotting sketches a hyperbola at the final stage, which is consistent with the Equation (2.31). Besides, both the highest velocity matches the theoretical. But there still exists some deficiency from the boundary deficiency though treatment is already applied to remedy it.

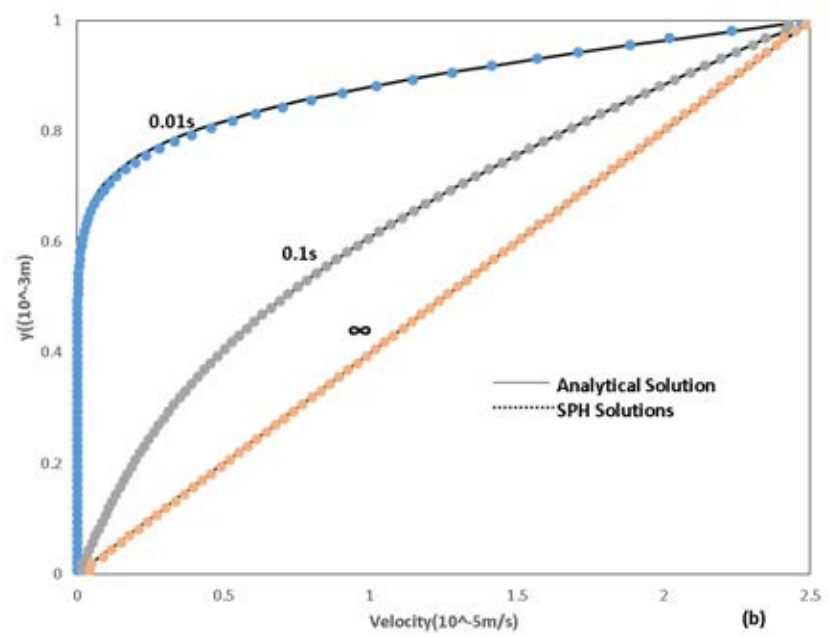
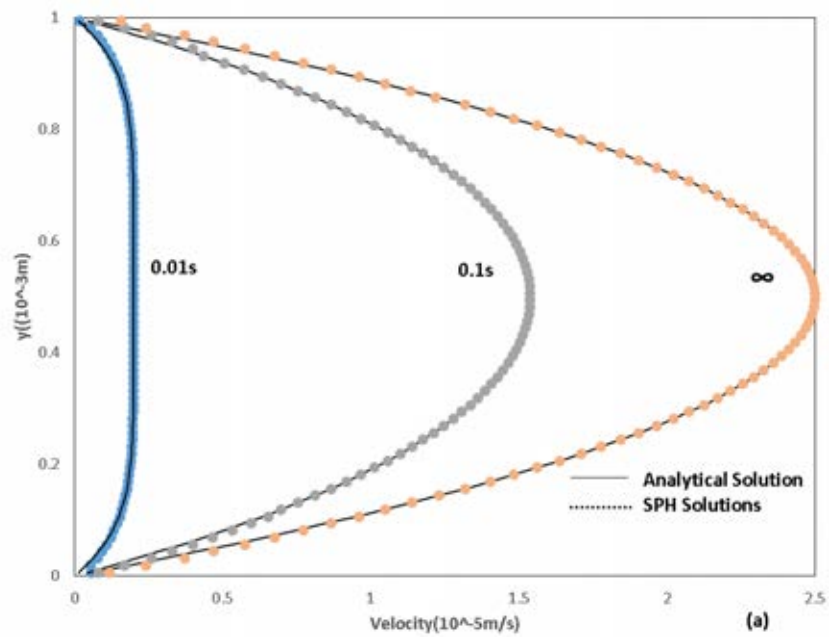


Figure.2.4 Fluid particle velocity profiles for (a)Poiseuille flow and (b)Couette flow at $t=0.01s, 0.1s, \infty$

2.8 Conclusions

This chapter provides a general introduction to the SPH and CGMD/MSM method and presents a common modelling process for conventional simulations with only SPH method. Two classical validation tests are implemented accordingly, with their results validated against the theoretical solutions.

Simulations with the coupling method principally follow the same routine in simulation conducted by SPH method, so no more iteration is made for this approach. Besides, owing to the various requirements for the specific simulation treatments, more detailed description about the practical choice for the coupled method is presented in the following chapters.

Chapter 3

SPH simulation of hydrodynamics within the GI tract using LAMMPS

Abstract

We developed a mathematical model that describes the motion of viscous fluids in the partially-filled large intestine caused by the periodic contraction of the elastic walls (peristalsis). In-vitro data are used to validate the model. The model is then used to determine the fundamental mechanisms of mass transport under the effect of various types of operating conditions and peristaltic waves. We identified two main transport mechanisms: the surfing mode and the pouring mode. The first mechanism is considerably faster than the second, but only involves the surface of the liquid. The second mechanism causes deeper mixing between adjacent pockets (haustra) and appears to be the main transport mechanism. In both cases, the fundamental parameter that determines the efficiency of mass transport is α , the fraction of mass that moves between two adjacent pockets during a peristaltic wave. Once this parameter is known, the transport in both the surfing and the pouring mode can be determined from first principles. In general, mass transport also depends on the shape of the peristaltic wave, as one might expect. Unexpectedly, however, this does not apply to the first pocket. This observation can have profound consequences on experimental practice. Tracers in PET-like

experiments, for instance, should not be injected in the first pocket, because this is not always a good proxy of the real colon.

3.1 Introduction

The understanding of how food and drugs are conveyed in the colon, or large intestine, can help the design of more effective medicines that are absorbed in specific areas of the intestine and have less side-effects. However, the mechanism of mass transfer in the colon under the effect of peristaltic waves is not well understood especially in the case of partially-filled intestine. In-vivo experiments are expensive and time consuming (Hur et al. 2011), while in-vitro models require a compromise between technical complexities and biological features (Guerra et al. 2012).

Nowadays, mathematical modeling and computer simulations have become a valuable investigation tool in medicine. *In-silico* models, in fact, are increasingly supporting traditional in-vivo and in-vitro models to achieve a better understanding of many physiological and biomechanics phenomena. Computational Fluid Dynamics (CFD), in particular, has proven itself a powerful tool in the study of transport phenomena in the GI tract (see Misra and Pandey 2006 for a review). In the majority of works, however, the external walls are considered rigid, and the fluid is not propelled by the contraction of flexible membranes as in the real case. Typical examples like simulations conducted by Kozu et al. (2010) and Schulze (2015), which focus more on the specific transport phenomena at certain local segments from large scale or the overall changes to certain

elements and neglects the detailed interaction information between the food content and the colons. One of the few exceptions is Sinnott et al. (2012) that couples Smoothed Particle Hydrodynamics (SPH) with a Mass-and-Spring representation of the membrane to study the hydrodynamics in flexible pipes subjected to peristaltic waves.

All these models refer to the case of completely fluid-filled intestine. However, most of the time the intestine is only partially filled and models that cover this case have not been developed yet. In this paper, we use an approach with some similarities to Sinnott et al. (2012) to derive a mathematical model that describes the motion in partially-filled flexible-ducts with peristaltic waves. In order to validate the model, we use data from an in-vitro colon model developed at the University of Birmingham.

The validated model is then used to address the following research question: “How can we improve the reliability of in-vitro models of the large intestine?” Considering that we know very little of the actual colon peristalsis, this seems a daunting task. Therefore, we attacked the problem from an unconventional angle. Instead of looking at the similarities between the in-vitro model and the real colon, we focused on the aspects of reality that the model *cannot* capture. We investigate the main features of the flow, and we identify the features of the in-vitro model with the highest probability of being different from the real case. Based on this knowledge, we suggest possible changes to improve the current experimental practice.

3.2 Modelling

3.2.1 Modelling approach

A hybrid computational methodology called Discrete Multi-hybrid System (DMHS) is used to simulate the motion of both the internal liquid phase, and the external flexible membrane of the intestine. Generally, the DMHS links different discrete (i.e. particle based) modelling techniques in order to reach results not attainable with each technique separately. For instance, the SPH method is less efficient in depicting the flexible membrane compared to the CGMD method. This method has been successfully tested for both solid-liquid flows (Alexiadis 2014, Alexiadis 2015a, Alexiadis 2015b) and fluid-structure interaction (Ariane et al. 2016). In this study, Smoothed Particle Hydrodynamics (SPH) is used to simulate the fluid, and Coarse Grained Molecular Dynamics (CGMD) the membrane. Since both these methods are particle-based, their coupling is computationally simple and efficient. This is an advantage over continuum-discrete two-way coupling, which require computational interfaces to connect the continuum and the discrete solvers as discussed in Alexiadis et al. (2013), Alexiadis et al. (2014), and Alexiadis et al. (2015).

In this study, specific models for solid contact/collision (e.g. the Discrete Element Method), or for fluctuating hydrodynamics (e.g. Dissipative Particle Dynamics) are not necessary; consequently, the coupling is limited to SPH (liquid phase) and CGMD (solid phase). As a consequence of this, the modelling approach resembles that of Sinnott et al.

(2012), with the difference both bond and angle potentials are used to model the membrane, whereas Sinnott et al. (2012) only uses bonds.

A brief introduction to both SPH and CGMD has been given in last chapter, together with the approach used to couple these two models. Specific details and other applications of the DMHS can be found in Alexiadis (2014), Alexiadis (2015a), Alexiadis (2015b) and Ariane et al. (2016). In previous DMHS publications, there is an interchangeable use of the terms CGMD and Mass-Spring Model (MSM). This depends on the fact that different scales are covered in these applications. Microscopic applications use proper CGMD, while macroscopic applications use MSM. They are mathematically equivalent, but MSM uses bond/angle/dihedral potentials only to model macroscopic elastic/bending/torsional properties of solids. In this paper, MSM is preferred, which is more consistent with the scale under investigation. In the following subsection, however, CGMD is used, which is more consistent with the original DMHS formulation.

3.2.1 Specific parameters used in DMHS method intestine simulation

In the last chapter, a detailed introduction of methodology is illustrated in subsection 2.2 and 2.3. In this chapter the so-called Lucy kernel function is chosen (Equation. 2.8) and the mass of each particle $m = 6.13 \cdot 10^{-5}$ kg, the initial distance among particles $\Delta r = 2.5 \cdot 10^{-4}$ m, the smoothing length $h = 2.5 \cdot 10^{-4}$ m and the time step $\Delta t = 10^{-5}$ s. Various expressions for the tensor $\Pi_{i,j}$ are available in the literature. Here the Morris' formulation is used for low Reynolds numbers (Equation. (2.20)). At each time step, Equation. (2.10) is used to update the velocities of the fluid particles, while their density can be calculated

either by Equation. (2.3), considering ρ as a normal scalar field, or, as done in Equation. (2.13) for this chapter, by means of the discrete approximation expression of the continuity equation.

The equation of motion is expressed by Equation (2.11) and the correlation between ρ and P is a necessary prerequisite to close it. In this chapter, Tait's equation (Equation (2.22)) is used to achieve this goal, where the parameters used here are $\rho_0 = 1000 \text{ kg m}^{-3}$ and $c_0 = 1 \text{ m s}^{-1}$.

The basic formation of coupling method has been explained from Equation (2.23) to Equation (2.26), and in this chapter the values for Equation (2.25) are $k_b = 10^{-4} \text{ J}$, $r_0 = 2.5 \cdot 10^{-4} \text{ m s}^{-1}$, $r_{max} = 4.5 \cdot 10^{-4} \text{ m s}^{-1}$, for Equation (2.26) $k_a = 8 \cdot 10^{-5} \text{ J}$, $\theta_0 = \pi/2 \text{ rad}$ to establish the model.

Same as the two methods, the coupling process can be achieved by means of satisfying several conditions briefly explained from Equation (2.27) to Equation (2.30) in last chapter, here the values for Equation (2.30) are $K = 10^{-10} \text{ J}$, $r^* = 2.5 \cdot 10^{-4} \text{ m}$.

3.2.2 Geometry

The geometry investigated here does not refer directly the large intestine, but to an *in-vitro* model of the intestine developed at the University of Birmingham.

A schematic representation of the experimental Dynamic Colon Model (DCM) model is presented in Figure 3.1c. The tube consists of ten segments with 20 cm total length and diameter 5 cm. Inflation and deflation of the membrane of each segment is performed by

controlling the back and forward displacements of a syringe using a stepper motor. Thus, synchronization of the oscillations of the segments was achieved resulting in producing an antegrade wave at a speed of 2 cm s^{-1} . This speed value represents the velocity observed in proximal colon of healthy humans based on manometric measurements (Dinning et al., 2014). At the end of the tube, a rigid siphon was placed which represents the hepatic flexure and keeps the fluids inside the DCM tube during propulsive waves generated by the wall motion.

The 2D geometry used in the simulation is described in Figure 3.1a, a channel is divided in $N + 1$ pockets (segments), of roughly elliptic shape, representing the intestine's haustra. these pockets are numbered from 0 to N ; their length is b , and the level of fluid in the channel L . The horizontal position of the pockets is measured from the centre of the first pocket. Therefore, the first pocket is located at $x_0 = 0$, the second at $x_1 = b$, and the k^{th} pocket at $x_k = kb$.

The fluid moves from one pocket to the other due to the contraction of the membrane (Figure 3.1b); when it reaches the last segment, it overflows and moves out of the computational domain. In the calculations, it will be assumed that all the fluid particles that exit the system are ideally collected in an hypothetical $(N+1)^{\text{th}}$ pocket located at $x_{N+1} = (N+1)b$.

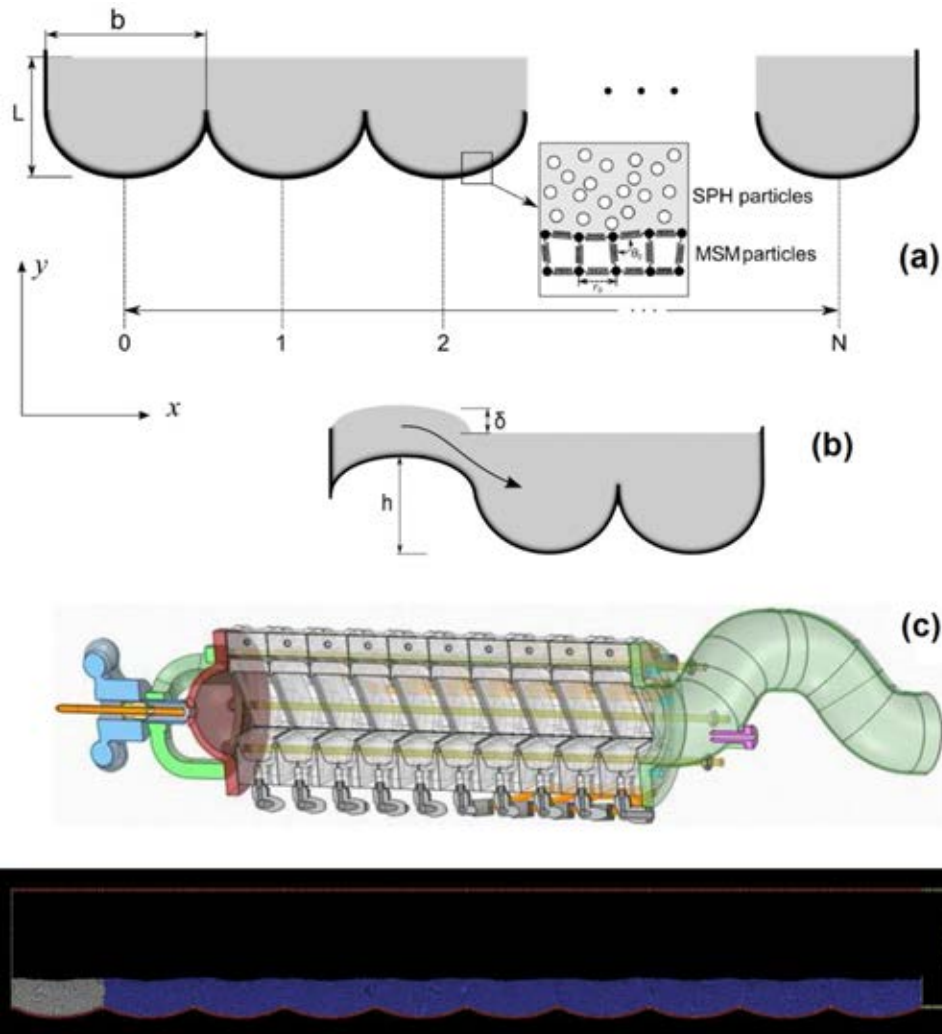


Figure 3.1 The geometry used in the simulation (a), the contraction of the pocket's membrane (b), the artificial colon model used in the experiments (c), and snapshot of the of simulations at time $t = 0$ (d).

The fluid is divided into SPH particles, whose number depends on the level of liquid in the channel. The membrane is divided in 5250 MSM particles distributed in three layers. The number of SPH particles used in the simulation is 19928, 3,756, 42344, and 59928 for respectively $L = 0.46, 0.81, 1.11,$ and 1.57 cm. Figure 3.1a also shows the springs-and-hinges structure (only two layers are shown) used to model the membrane and a thorough discussion is made concerning bond (springs) and angle (hinges) potentials in section 3.2.1. Only the lower membrane is taken into account. Since this study only deals with the partially filled intestine; the upper membrane is not required.

Figure 3.1d shows the geometry used in the simulation. A wall bounds the first pocket on the left, while an overflow allows the fluid to exit the channel from the right. The role of the white particles is discussed in Section 3.2.4.

3.2.3 Peristaltic wave

Muscles contracts in sequence to produce a peristaltic wave, which propels the digesting food along the intestine. The exact dynamics of real peristaltic waves is still unknown. In the simulations, therefore, the peristaltic wave used in the artificial colon model is studied. In Section 3.4.5, however, the effect of a different type of wave will be investigated.

In the experimental apparatus (Figure 3.1c), the segments move with a predetermined pattern that produces an artificial peristaltic wave. The same pattern in the computer simulations (see Figure 3.2) is recreated.

- At time $t=0$, all the pockets are in their relaxed state and no force is applied.
- At time t_w , a force in the upper direction is applied to the first pocket and a downwards force to the second pocket.
- At time $2t_w$, the upwards force is maintained to keep the membrane of the first pocket at its highest location, while the downwards force is released so that the second pocket gradually returns to its equilibrium configuration.
- At time $3t_w$, the force on the first pocket is released, an upwards force is applied to the second pocket, and a downward force to the third.

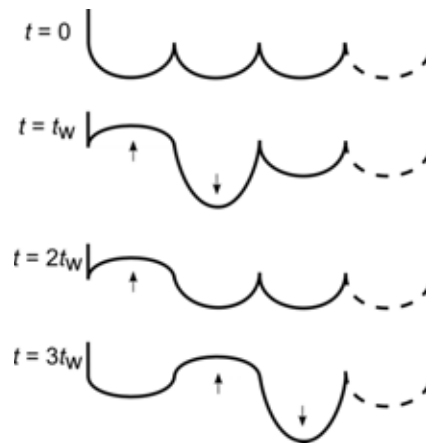


Figure. 3.2 Schematic representation of the progressive contractions and expansion of the membrane sections during the peristaltic wave.

The configuration at time $3t_w$, therefore, is the same of time t_w only shifted by one pocket (Figure 3.2). The configuration at time $4t_w$ will be the same of that at time $2t_w$, only shifted by one pocket and so on. In this way, all the pockets progressively contracts and expand recreating the type of peristaltic wave used in the experiments. Figure 3.3 shows the overall propagation of the wave as result of the sequence of contractions and expansions. Table 1 illustrates the same concept in matrix notation; 1 indicates an upwards force applied to a particular pocket at a specific time, -1 indicates a downwards force. As Table 3.1 indicates, every 2 rows, the same pattern is shifted by one column and repeated.

period \ pocket	0	1	2	3	4	...	N
0	0	0	0	0	0	...	0
t_w	1	-1	0	0	0	...	0
$2 t_w$	1	0	0	0	0	...	0
$3 t_w$	0	1	-1	0	0	...	0

$4 t_w$	0	1	0	0	0	...	0
$5 t_w$	0	0	1	-1	0	...	0
$6 t_w$	0	0	1	0	0	...	0
...
$(2N+5) t_w$	0	0	0	0	0	...	1

Table 3.1 Matrix representation of the peristaltic dynamics

Each time interval t_w is named as a *sub-period* of the wave. If we look at each column in Table 3.1, it can be seen that during a peristaltic wave, each pocket has a recurrent dynamics of the type $[-1, 0, 1, 1]$. This dynamics last for four sub-periods and it is called *haustum-period* here. The contraction of all the $N+1$ pockets takes $T_w=(2N+5)t_w$, which is called *peristaltic-period*. After the whole wave is completed, the process restarts with a new peristaltic wave. In this work, each simulation is composed of 10 peristaltic waves. The peristaltic velocity is defined as the ratio between T_w and the total length of the channel $(N+1)b$

$$V_w = \frac{(N + 1)b}{T_w}. \quad (3.1)$$

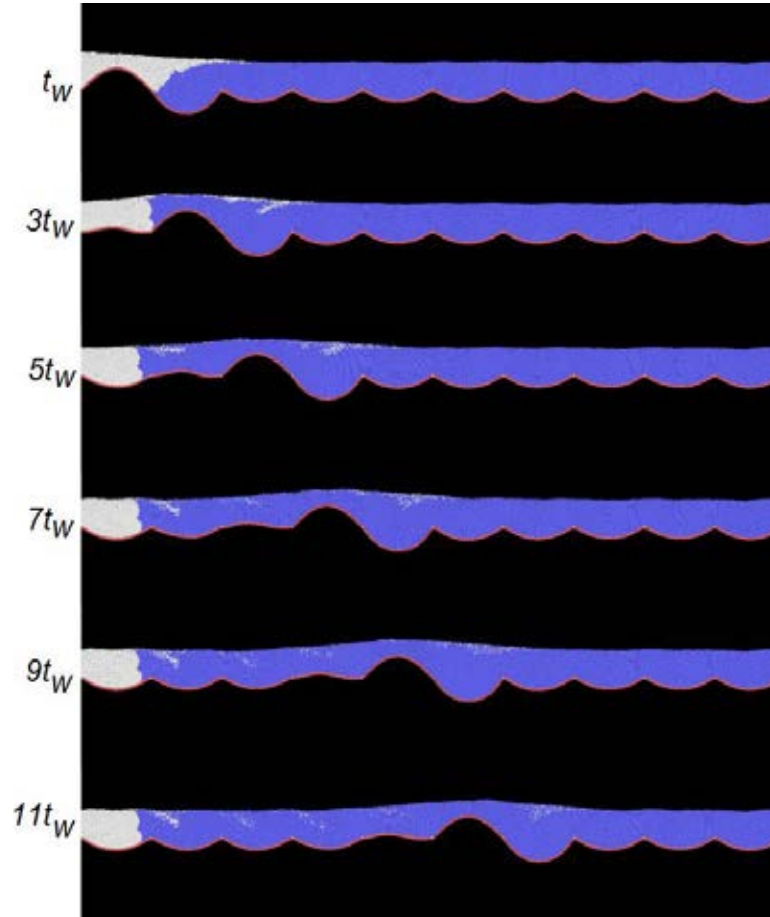


Figure. 3.3 Simulation snapshots illustrating the fluid motion induced by a peristaltic wave for $\nu = 10^{-6} \text{ m}^2 \text{ s}^{-1}$, $L = 1.11 \text{ cm}$ and $V_w = 1.45 \text{ cm s}^{-1}$. The tracking (white) particles partially mix with the fluid of other pockets (pouring mode) and partially advance on the surface of the channel (surfing mode). The fluid that moved in the second pocket at t_w partially flows back into the first pocket at $3t_w$ (ineffective surfing). See Section 3.2.4 for details on these three propagation modes.

3.2.4 Preliminaries and dimensionless analysis

In order to study mass propagation in the channel, *tracking particles* are introduced in the first pocket at the beginning of the simulation. These are SPH particles with exactly the same properties of those in the rest of the flow. They can be distinguished because they have a different colour in the snapshots (Figure 3.3) and their trajectories can be tracked during the simulation. The number of tracking particles (n_p) depends on the total number

of SPH particles (n_{TOT}) of the simulation. This value is not fixed since it varies with L ; in general, however, $n_P = n_{TOT} / (N+1)$.

In order to study the propagation of mass within the system, the concept of *front penetration* (x_F) and *front velocity* (u_F) is introduced. If the ordinate of a particle i at time t is x_i , the front penetration is defined as

$$x_F = \sum_{i=0}^{n_P} \frac{x_i}{n_P}, \quad (3.2)$$

which represents the average location of all the tracking particles. In principle, the front velocity u_F should be simply the time derivative of the front position x_F . However, since the peristaltic wave causes discontinuous front propagation, it is more practical to define u_F on the basis of the front penetration at the end of one peristaltic period, i.e.

$$u_F = \frac{x_F(t = T_w)}{T_w}. \quad (3.3)$$

Given a L (liquid level, see Figure 3.1a), h (membrane uplift, see Figure 3.1b), ν (kinematic viscosity) and V_w (speed of the peristaltic wave, Equation. 3.1), the calculation of u_F that provides information on how mass propagates along the channel. The parameter b should also have been included (distance between pockets, see Figure 3.1a), but since the geometry of the experimental apparatus is fixed, it is considered constant (2 cm). According to the Buckingham π theorem there are four fundamental dimensionless groups: Re (Reynolds number) helps the prediction of the flow pattern, Ga (Galileo number) is adopted in describing viscous flow, Fr (Froud number) indicates the flow

condition of waves and Λ (geometric ratio) denotes the geometric similarity. They are defined as follows

$$Re = \frac{bu_F}{\nu}, Ga = \frac{h^3 g}{\nu^2}, Fr = \frac{V_w}{\sqrt{gh}}, \Lambda = \frac{h}{L}. \quad (3.4)$$

The forces that generate the peristaltic wave and the elastic properties of the membrane are not directly accounted in these four dimensionless groups. However, these are already comprised in the variable h that indicates the maximum height at which the membrane is lifted by the applied force F . This analogous F is calibrated to achieve a final membrane displacement (h) of around 1 cm, as observed in the experiments.

3.3 Results

3.3.1 Simulations

There are two types of parameter required for the simulations: model parameters and simulation parameters. The first group consists of internal parameters used by the SPH and MSM solvers; the second refers to the operative conditions. This Section focuses on the second group (i.e. L , h , ν and V_w); the other parameters can be found in section 3.2.

A large number of simulations are carried out to cover various operative conditions; ν was varied between $0.5 \cdot 10^{-6}$ and $500 \cdot 10^{-6} \text{ m}^2 \text{ s}^{-1}$, V_w between 4.3 cm s^{-1} and 26.1 cm s^{-1} , L between 0.46 and 1.6 cm, h between 0.88 and 1.16 cm. In total, 104 simulations are carried out. Each simulation lasted for ten peristaltic waves. With respect to the fundamental dimensionless groups identified in Section 3.4, the simulations cover the following ranges: $Ga = 23\text{--}5 \cdot 10^7$, $Fr = 0.023\text{--}0.15$, $\Lambda = 0.5\text{--}1.9$.

3.3.2 Validation

In order to validate the model, the simulation results are compared with experimental data. Positron Emission Tomography (PET) system developed in University of Birmingham was used in order to assess the mixing process within the DCM tube under anterograde waves. Details of the PET system can be found in (Broadbent et al. 1993). Half prefilled DCM tube was placed between the two positron cameras and 1 mL of radiolabelled water was injected in the first segment. Ten antegrade waves, with 10 s time delay between them, were applied. The duration of each frame (Figure 3.4) was 1 s. Results of the concentration distribution of the radioactive solution in grayscale values vs distance along the x axis in pixels size (0.25 mm) were plotted. The grayscale value of each pixel is the mean of the vertical pixel intensities within the tube at each point.

The number of tracking particles in the simulations are compared with the concentration of the radioactive tracer in PET experiments at approximately the same conditions and after the same number of periods (Figure 3.4).

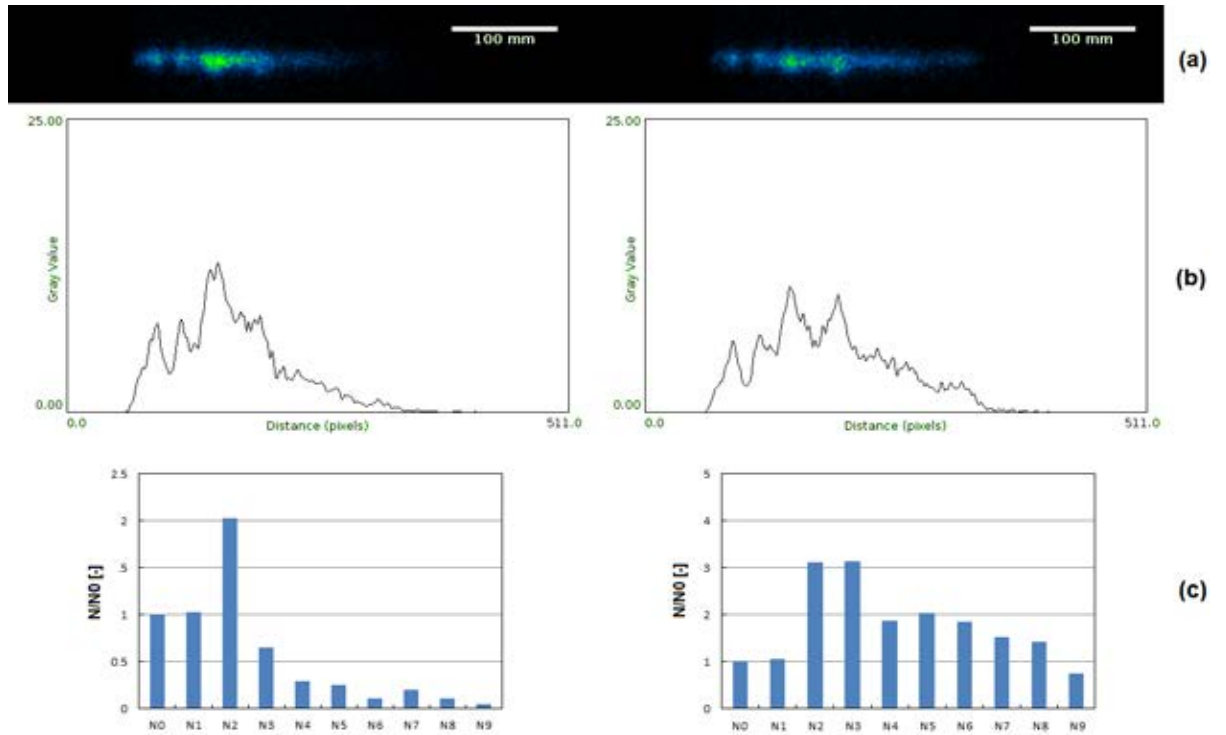


Figure 3.4 PET images: greyscale distribution plots (b), generated from the experimental data (a), compared to dimensionless concentration N/N_0 of tracker particles in the simulations (c) after 5 and 7 peristaltic waves ($\nu = 10^{-6} \text{ m}^2 \text{ s}^{-1}$, $L = 0.8 \text{ cm}$, $V_w = 1.45 \text{ cm s}^{-1}$). The concentration N_0 in the first pocket has been normalized to match the experiments and the distribution rescaled accordingly. Units between (b) and (c) are therefore different. Distributions (b) are continuous and indicate the tracer concentration along the whole channel. Distributions (c) are discrete and indicate the concentration of white particles in each pocket.

In general, the comparison shows a good agreement between experimental data and calculations. The only exception occurs in the first pocket, which shows considerably higher concentrations in the simulations. This is probably due to the fact that the simulations and the experiments have two very different methodologies to ‘initialize’ the tracking fluid in the first pocket. In the simulations, all the particles of the pocket are simply attributed to the tracking set. In the experiments, the radioactive compound is injected from above into the first pocket that is already filled with liquid. If the first segment is normalized (N_0 in Figure 3.4) to match the simulation with the experiments

and rescale the distribution, however, the results are very similar as indicated by Figure 3.4.

3.3.3 Method for calculating the front velocity (u_F) from the simulations

Figure 3.5a shows how x_F varies with time for the case of $L= 0.46$ cm $\nu = 2 \cdot 10^{-6}$ m² s⁻¹, $V_w = 1.45$ cm s⁻¹. The propagation has an irregular profile. The tracking particles, driven by the peristaltic wave, move in a pulse-like manner. The simulations were carried out for ten waves, and can be distinguished in Figure 3.5 exactly ten pulses. A simple way to calculate the front velocity u_F is to determine the linear least-square approximation of x_F (dotted lines in Figure 3.5): the slope of this line provides u_F . In certain cases, however, linear fitting is not satisfactory. Figure 3.5b, for instance, shows the simulation for $L = 0.81$ cm $\nu = 1.6 \cdot 10^{-6}$ m² s⁻¹, $V_w = 1.45$ cm s⁻¹. Linear fitting is adequate only for the first 80 s. After 80 s, a significant amount of fluid has left the channel and the level L has decreased. Generally, it can be observed that front propagation is faster at lower L . Figure 3.5b graphically depicts this series of events. After 80 s, L decreases because fluid exits the channel and, consequently, the slope increases. However, when the level decreases below a certain threshold, the fluid in each pocket remains trapped in isolated pools. In this case, the velocity propagation drops. Figure 3.5c ($L= 0.46$ cm $\nu = 10^{-6}$ m² s⁻¹, $V_w = 1.45$ cm s⁻¹) illustrates this: after 40 s, u_F gradually decreases due to the formation of separated liquid pools.

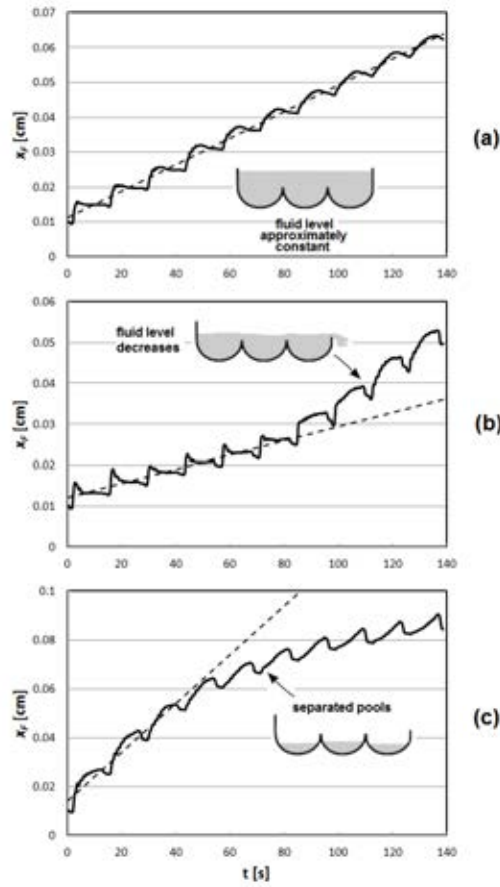


Figure. 3.5 Front penetration x_F versus time for the cases: $L= 0.46$ cm $\nu = 2 \cdot 10^{-6}$ m² s⁻¹, $V_w = 1.45$ cm s⁻¹ (a), $L= 0.81$ cm $\nu = 1.6 \cdot 10^{-6}$ m² s⁻¹, $V_w= 1.45$ cm s⁻¹ (b) and $L= 0.46$ cm $\nu = 10^{-6}$ m² s⁻¹, $V_w= 1.45$ cm s⁻¹ (c)

In the next Sections, u_F is calculated from the simulations. In the cases where the slope is not constant, the initial slope is used as illustrated in Figure 3.5. This convection is adopted because the real intestine is considerably longer than our model and, therefore, the level of liquid is not expected to change as quickly as in the simulation.

3.4 Discussion

Visual observation (e.g. Figure 3.3) shows that there are at least two simultaneous modes of front propagation. In the first case, which we called the *pouring mode*, the peristaltic wave pushes the fluid from one pocket to the next causing a certain level of mixing. Each

time the tracking particles move to a new pocket, a certain number of them are left behind and remain in the previous pocket. In the second mode, which is called the *surfing mode*, most of the motion occurs on the surface without appreciable mixing with the bulk. In this case, the tracking particles can move longer distances by surfing over the surface of the liquid. However, the surfing mode can be affected by backflow that occurs during the lifting of the membrane. The interaction of surfing and backflow originates a third sub-mode that is named *ineffective surfing*. This Section discusses these three possibilities in detail.

3.4.1 Pouring Mode

The pouring mode arises when some mixing occurs within each pocket. Initially, all the tracking particles n_P are located in the first pocket. At the end of a haustum-period, a fraction α of particles has moved from the first to the second pocket. This fraction includes both the effect of forward motion caused by the contraction of the first membrane, and the effect of backflow caused by the contraction of the third membrane (Figure 3.6).



Figure. 3.6 Schematic representation of the pouring mode

During the next haustum-period, a fraction α of particles leaves the second pocket and goes into the third pocket. Assuming that α remains constant, the particles in the third pocket are now $\alpha^2 n_P$ and those in the second pocket $(1-\alpha)\alpha n_P$. By following the same logic, it can be inferred that the number of particles in the k^{th} pocket at the end of the j^{th}

period. As an example, Table 3.2 shows how the number of particles changes in the first 4 pockets during the first 3 haustrum-periods.

	$k=0$	$k=1$	$k=2$	$k=3$
$j=0$	n_P	0	0	0
$j=1$	$(1-\alpha)n_P$	αn_P	0	0
$j=2$	$(1-\alpha)n_P$	$\alpha(1-\alpha)n_P$	$\alpha^2 n_P$	0
$j=3$	$(1-\alpha)n_P$	$\alpha(1-\alpha)n_P$	$\alpha^2(1-\alpha)n_P$	$\alpha^3 n_P$

Table 3.2 Number of particles in the first 4 pockets during the first 3 haustrum-periods for the pouring mode

On the basis of these considerations, the front position can be derived at the end of the peristaltic wave for the pouring mode

$$x_P = \sum_{k=0}^N \frac{bk(1-\alpha)\alpha^k n_P}{n_P} \quad (3.5)$$

In equation (3.5), instead of using x_i to calculate the average position of the tracking particles (as done in eq. 3.2), the approximation is made of the position of all the particles contained in the k^{th} pocket with the position kb of the pocket.

The series in eq. 3.5 has solution

$$x_P = \frac{\alpha - (N+1)\alpha^{N+1} + N\alpha^{N+2}}{(1-\alpha)} \quad (3.6)$$

which, since $\alpha < 1$ and N is a relatively large number (here $N=9$), can be further simplified to

$$x_P \cong \frac{\alpha}{1-\alpha} b \quad (3.7)$$

and finally

$$u_p = \frac{\alpha}{1 - \alpha} \frac{b}{T_w} = \frac{\alpha}{1 - \alpha} \frac{V_w}{N + 1} \quad (3.8)$$

3.4.2 Surfing mode

In this case, the tracking particles from the first pocket slide above the surface of the second, and stop only after they surpass the centre of the pocket (Figure 3.7).

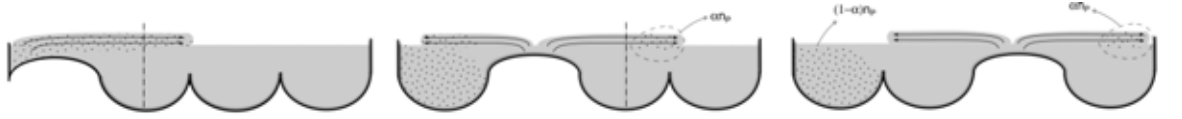


Figure. 3.7 Schematic representation of the surfing mode

In this way, during the following haustrium-period, the flow from the second pocket pushes the tracking particles further forwards. In the most extreme case, all the particles αn_p , which left the first pocket initially, are pushed further to the third pocket. From the third pocket, they are pushed to the fourth and so on. One period after the other, the particles keep surfing forwards in synchrony with the peristaltic wave. At the end of the wave, the position of the front is simply the average between the particles remained in the first pocket (positions x_0), and those that exit the system after surfing over the entire channel surface (positions x_{N+1}).

$$x_S = \frac{(1 - \alpha)n_p x_0 + \alpha n_p x_{N+1}}{n_p} \quad (3.9)$$

Equation (3.9) can be further simplified. As discussed in Section 3.2.2, in fact, $x_0 = 0$ and $x_{N+1} = (N+1)b$. Introducing these values in Equation (3.9), it can be obtained that

$$x_S \cong \alpha b(N + 1). \quad (3.10)$$

As before, the front velocity is calculated by dividing Equation (3.10) by T_w

$$u_S = \frac{\alpha a(N + 1)}{T_w} = \alpha V_w. \quad (3.11)$$

The fast front propagation of the surfing mode should be considered as an extreme and idealized case. If an assumption is made that a typical value of $\alpha=0.1$, and $N=9$ as in our simulations, u_S is around one order of magnitude larger than u_P . The computer simulations, however, show that the actual value of u_F is generally closer to u_P than u_S .

The calculation of both u_P and u_S requires information concerning α . In this paper, α is taken from the simulation by counting the number of tracking particles in the first pocket after one haustum-period. Alternatively, α can also be measured experimentally.

3.4.3 Ineffective surfing mode

The surfing mode bases its effectiveness on the fact that, at each period, the front surpasses the centreline of the next pocket. In this way, it is always ideally located to catch the next wave and advance further. However, if the fluid is highly viscous, it does not move far enough to reach the centreline. Therefore, when the membrane of the next pocket goes up, the tracking particles are caught in the backflow and, instead of advancing, they are pushed back into the previous pocket (Figure 3.8). This is also an idealized situation, where the particles go back and forth from the first to the second pocket without actually propagating along the channel and, therefore, $u_I = 0$, where u_I is the front propagation for ineffective surfing.



Figure. 3.8 Schematic representation of ineffective surfing

A general criterion can be established to determine whether, given a certain fluid viscosity, the surfing mode is effective or ineffective. Starting point is the Navier-Stokes equation where only the transient and the viscous terms are considered.

$$\frac{du}{dt} - \nu \frac{d^2u}{dx^2} = 0. \quad (3.12)$$

Based on the order of magnitude, the time τ is estimated that a fluid with initial velocity u will take to rest

$$\frac{u}{\tau} = \nu \frac{u}{b^2}, \quad (3.13)$$

and therefore

$$\tau = \frac{b^2}{\nu} \quad (3.14)$$

During this time, the front propagation advances of Δx_F under the effect of u_F and, therefore,

$$\Delta x_F = \tau u_F \quad (3.15)$$

Combining Equation (3.14) and (3.15), we obtain

$$\Delta x_F = \frac{u_F b^2}{\nu} \quad (3.16)$$

As explained above, surfing is effective only when the propagation pulse brings the tracking particles beyond the centreline of the next pocket ($\Delta x_F > b$, from the centreline of the first pocket to the centreline of the second pocket). If this does not happen, the backflow brings all the particles back to the initial pocket. This means that the surfing mode is effective only if

$$\frac{u_F b^2}{\nu} > b, \quad (3.17)$$

which means $Re > 1$. When this condition is met, ineffective surfing not only contrasts the effect of the surfing mode, but it can also act against the pouring mode as illustrated in Figure 3.3.

3.4.4 The dominant mode

The propagation velocities u_P , u_S and u_I refer to idealized situations. The actual front velocity u_F is expected to be a combination of the modes discussed above. The simulations show that the dominant mode is the pouring mode, and generally u_P is of the same order of magnitude of the final front velocity u_F . In combination with the pouring mode, surfing can be either effective or ineffective; in the first case $u_F > u_P$, in the second $u_F < u_P$. Figure 3.9 compares the Reynolds number calculated using the actual velocity u_F (Re in Equation (3.4)) with that calculated using u_P (substitute u_P with u_F in Equation. (3.4)).

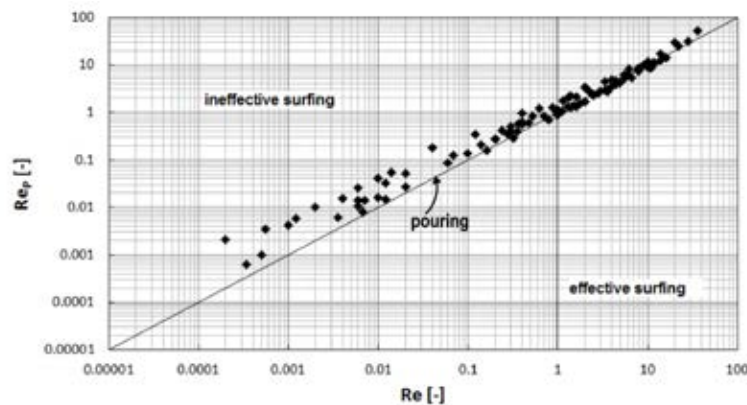


Figure. 3.9 Reynolds number calculated using u_F (Re) versus Reynolds number calculated using u_P (Re_P).

Data close to the are those where $u_F \sim u_P$. In general, u_P provides a good approximation of u_F for $Re > 1$. In some simulations u_F is slightly higher than u_P (effective surfing), but

this only happens at low viscosities ($\nu \leq 2 \cdot 10^{-6} \text{ m}^2 \text{ s}^{-1}$). However, for $\text{Re} < 1$, u_F becomes gradually smaller than u_P , which is consistent with our proposed criterion for ineffective surfing.

3.4.5 Effect of the type of peristaltic wave

The actual shape of the peristaltic wave in the intestine is unknown. In the previous sections, various wave speeds V_w were compared, but the shape of the wave was always the same. Therefore, the investigation into a different type of shape was carried out to assess the impact of the wave shape on mass propagation. Table 3.3 shows the matrix representation of this new wave. In the old wave, the contraction of each membrane section was maintained for two periods, in the new wave it is maintained for five periods (see also Figure 3.10).

period pocket	0	1	2	3	4	...	N
0	0	0	0	0	0	0	...
t_w	1	-1	0	0	0	0	...
$2 t_w$	1	0	0	0	0	0	...
$3 t_w$	1	1	-1	0	0	0	...
$4 t_w$	1	1	0	0	0	0	...
$5 t_w$	1	1	1	-1	0	0	...
$6 t_w$	0	1	1	0	0	0	...

$7 t_w$	0	1	1	1	-1	0	...
$8 t_w$	0	0	1	1	0	0	...
$9 t_w$	0	0	1	1	1	-1	...
...

Table 3.3 Matrix representation of the new peristaltic wave. The differences between the old and new wave are highlighted in bold.

The new wave were repeated the same 104 simulations carried out for the old wave. At any given time, more membrane segments are contracted in the new wave (Figure 3.10).

This confers a higher “squeezing power” to the wave that propels more fluid forwards.

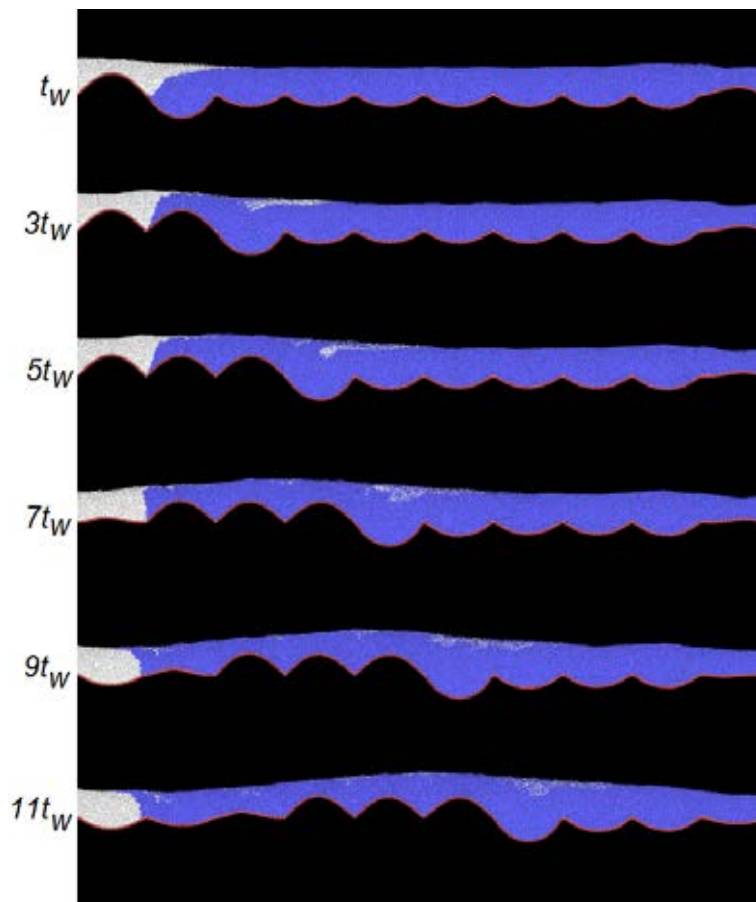


Figure. 3.10Simulation snapshots of the new peristaltic wave ($\nu = 10^{-6} \text{ m}^2 \text{ s}^{-1}$ and $L = 1.11 \text{ cm}$).

In many cases, however, the new wave does not radically change the front velocity. Figure 3.11 (new wave graph) illustrate this point. At around 40 s, it indicates a (least-square) slope increase, which indicates a decrease in the level of liquid as discussed for Figure 3.5. After 100 s, the system reaches a plateau, which indicates the formation of isolated pools.

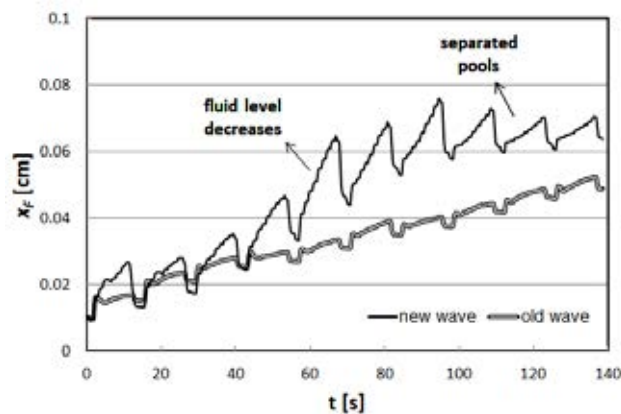


Figure. 3.11 Front propagation in the case of $v = 10^{-6} \text{ m}^2 \text{ s}^{-1}$ and $L = 1.11 \text{ cm}$:
old wave versus new wave.

Conversely, the level in the old wave does not change as much, and the profile maintains a linear behaviour. All this is consistent with the fact that the new wave pushes more fluid out of the channel. However, if the observation just includes the first 40 s, when the fluid level is comparable for both cases, the slope is similar. This means that the different dynamics depends on the change of level rather than the shape of the wave. Moreover, since the calculation of u_F is based on the initial slope, the front propagation in the two cases does not change significantly. If the equivalent to Figure 3.9 is drawn for the new wave, in fact, the main features of the two graphs would remain the same.

It may look like a contradiction that the new wave drives more fluid out of the channel but, at the same time, the front velocity remains roughly the same. The explanation depends on the fact that all the tracking particles are initially located in the first pocket. The net flow rate in the first pocket is lower than that of the other pockets because (using Figure 3.1d as reference) the first pocket has only one neighbour on the right, while, on the left, is constrained by a wall. Therefore, there is no inflow from the left that pushes the tracking particles forward, but there is backflow from the right that moves back some particles that had left the pocket during the previous haustrium-period.

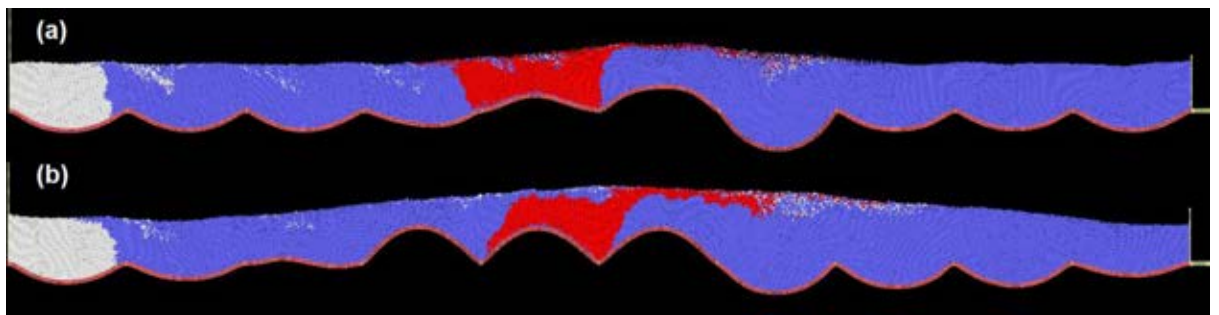


Figure. 3.12 Propagation of tracking particles starting in the first pocket (white) and fifth pocket (red) in the case of $v = 10^{-6} \text{ m}^2 \text{ s}^{-1}$ and $L = 1.11 \text{ cm}$: old wave (a) versus new wave (b).

In Figure 3.12, a second type of tracking particles (red) is used. These particles initially are located in the fifth pocket. Comparison is made during the propagation of red and white particles after the first peristaltic wave crosses the fifth pocket. There is no big difference between the distribution of white particles between Figure 3.12a and Figure 3.12b. This confirms the observation obtained from Figure 3.11. However, the number of red particles leaving the fifth pocket can be up to ten times larger for the new wave. The observation shows, in particular, that the surfing layer is considerably thicker. This implies that, in the case of the new wave, the first and the fifth pockets are not

hydrodynamically equivalent. In the real colon, there is no wall on the side of the first pocket and the dynamics is likely to be closer to that of the fifth pocket rather than the first. This observation has important repercussions on the way we should design our experiments. Radioactive tracer in PET experiments, for instance, should not be injected in the first pocket, because this is not always a good proxy for the motion in the colon.

3.5. Conclusions

In this chapter, a computational model is devised for peristaltic motion including flexible boundaries and partially-filled intestine. This fills a gap in the literature. Previous works only deal with completely filled intestine, but for most of the time the intestine is only partially filled.

The model is validated with experimental data and applied to cases of practical interest. In particular, insights into the hydrodynamics of the large intestine are provided and the identified main hydrodynamic features of an in-vitro model developed at the University of Birmingham. Based on this information, it can provide some suggestion to some improvements in the design of in-vitro models and experimental practice. Two aspects, in particular, deserve attention.

Firstly, u_P can be calculable, which provides a reasonable approximation of the front propagation u_F , once the value of α is known. α can be easily measured from experiments. It only requires observations from one pocket; a large experimental apparatus, therefore, is unnecessary.

Secondly, a relatively short experimental apparatus can be used, but not all the pockets are equally good proxies of the colon. In general, the first pocket is not. As a consequence, in PET-like experiments, where the time evolution of a luminescent or radioactive compound is tracked, the tracer should not be injected in the first segment (the best choice depends on the type of wave).

Chapter 4

SPH simulation of hydrodynamics within the deep vein valves using LAMMPS

Abstract

The Discrete Multi-physics method, together with a customized agglomeration algorithm designed for blood clotting procedure, is adopted for the simulations with blood flows develops in deep venous valves. Development for flows under various valve conditions are investigated and compared. The results indicate that both the flexibility and the lengthiness of valve membranes have critical impact on the mechanical stress and blood agglomeration in blood flows. Specifically, although the inflexible and short leaflets result in insufficient inhabitation for back-flow and consequently the blood transportation efficiency is reduced; thus the risk of blood clotting formation is greatly declined by reducing the stagnant blood region. Moreover, in spite of the great influence of mechanical stress, the retention time plays a more determinative role in the process of the clots agglomeration.

4.1 Introduction

Blood clots frequently take place inside the deep veins (Kyrle and Eichinger, 2005). It behaves as the impediment against the blood flows and the proliferation of clots on valves will lead to severe occlusion which will strongly impair the function of valves.

Deep venous thrombosis (DVT) is a serious and painful disease, just as its name implies, forms from the clotting of blood develops in deep veins (Figure 4.1). If these clots become unstable and detached from the thrombus they can be delivered to the lungs, leading to a acutely lethal neopathy called pulmonary embolism (PE) .They have a collective name called VTE (venous thromboembolism), and statistics shows that it results in about 25,000 deaths per year in UK, which is approximate five times the combined number of deaths from breast cancer, acquired immunodeficiency syndrome and road accidents (Hunt et Al. 2009).

The accurate mechanisms of clot development in veins has remained inconclusive so far but researchers suspect that the specific flow patterns in veins, especially those around the valve flaps, play a fundamental role (Bovill and van der Vliet 2011). Another major cause of DVT is long-term limited mobility (e.g. post-operative on-bed rehabilitation, motor paralysis and long-time aircrafts). The insufficient efficacy of the muscle pump, namely, the incomplete assistance in blood flow through the veins leads to sluggish flows.

Furthermore, once a patient received success treatment after diagnosed as DVT, another thrombosis is easily prone to develop, which indicates that the special geometry of vessel,

as well as the specific bloodstream conditions, is a conducive factor to the formation of thrombus.

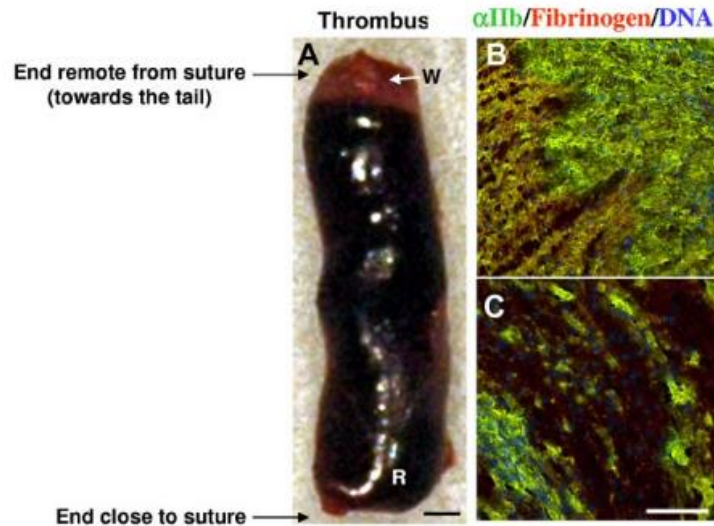


Figure. 4.1 A photograph and microscopic images of a thrombus that has formed in a mouse after venous constriction, with platelets (α IIb) binding to deposited fibrinogen (Brill et al. 2011)

Nowadays, modelling and simulation of the blood flow in deep veins and arteries can provide a fundamental contribution to deepen the exploration of association between disease under investigation and blood dynamics, as it gives details on both the haemodynamics and the valve dynamics. However, compared to the wide investigation of blood flow modelling and valve deformation for cardiac systems (Bavo et al., 2016; Borazjani, 2015; Fenlon & David, 2001; Halevi et al., 2015; Marom, 2015; Miandehi et al., 2015; Morbiducci, Ponzini, Gallo, Bignardi, & Rizzo, 2013; van Loon, 2010), few attention has been paid to venous valves.

The first numerical exploration of blood flow on vein valve was based on a Lagrangian approach (Buxton and Clarke 2006) and only focused on velocity variations at normal

conditions. In this study, the fluid was implemented using a Lattice Boltzmann (LB) model and the structure with a lattice spring model (LSM). Later, Zervides et al. (2008) adopted a one-dimensional electrical model to study the dynamic pressures applied to veins and quantify the differences of the pressure existing in a system including valves. While Wijeratne and Hoo (2008) using co-simulation such as the Arbitrary-Lagrangian-Eulerian (ALE) method explored vortex formation in sinus region and their detrimental impact on flow regulation in a symmetrical 2D model. However, the absence of valve flexibility in most models results in the missing interaction between bloodstream and the vascular valve. Lately, the squeezing of the wall and clot formation were integrated via the Fluid Structure Interaction (FSI) method by Simao et al. (2016). In this Eulerian approach, clots were simulated by the modification of the fluid viscosity. The results have shown the importance of the presence of solid aggregates and their implications for valve disorder. However the accuracy of discussion suffers from the geometry deficiency and short cycle duration mainly owing to the native disadvantage of the FSI method. Tricky problems also exist in other investigations, for instance, the overcomplicated algorithm for the reliable models, the coordination of the period of re-meshing and the insufficient vascular valve cycle (Van Loon et al. 2010, Kamensky et al. 2015).

In a previous study (Ariane et al., 2016), a model based on the discrete multi-physics (DMP) approach was proposed for modelling biological valves. This work has the advantage of allowing solid agglomeration, which is beneficial for its extension for models to the case of DVT in this chapter.

In particular, attempts are made to find an explanation for how mechanical stresses are distributed in the valve and what regions on the membrane where thrombi are most likely to form and grow potentially. By means of the investigating into several cutting points, the size and the flexibility of the venous valves, together with the inflow velocity, their determining role is revealed by the neighbouring haemodynamic around the leaflets.

This chapter is organized as follows. In the first part, the impact of the mechanical stress and the resident time in a stagnant area are brought into focus. Next, a discussion is made about how these parameters are affected by the geometry and flow conditions. Finally, an agglomeration algorithm is introduced in the model and analyse the agglomeration dynamics below the leaflets. Different from the FSI method, the adoption of discrete multi-physics approach means that the stability algorithm is no longer needed and introduces a more flexible treatment to the solid-liquid interaction via new algorithm.

4.2 Modelling

4.2.1 Modelling approach

The discrete multi-physics approach adopted here is based on the discrete multi-hybrid system (DMHS) method. Detailed information of this methodology has been clearly explained in chapter 2, to avoid repetition, no further depiction this method is given here.

This technique combines various mathematical models to achieve a representation of fluid-structure interactions and solid-liquid systems that is not attainable with each model separately.

In the DMHS model, the liquid portion, namely, the idealized blood is divided by many discrete particles in SPH method (Liu & Liu, 2003; Monaghan, 1992; Morris, Fox, & Zhu, 1997), while the solid structure is segmented into many conceptual node particles. Compared to the models for intestine used in last chapter, more specific computational connection between particles are established by two parts, one is the notional springs for modelling the elastic modulus and another notional chains for modelling the bending modulus. The treatment style is mathematically resembles the molecular bonds used in Molecular Dynamic (MD) method. Though similar to the CGMD method used for intestine in last chapter, the choice of Mass-Spring model (MSM) here is owing to scale difference.

4.2.2 Geometry

A 2D geometry used in the simulation of venous valve in lower extremity (Wijeratne and Hoo 2008) is described in Figure 4.2. The channel thickness is $h = 0.008$ m, the valve chamber diameter is $D = 0.014$ m and its length is $W = 0.04$ m. The length L is regarded as a vital geometry factor for the haemodynamic, and thus three values are chosen for the comparison: long (0.0256 m), medium (0.0175 m) and short (0.01 m). The definition of the area between two valves as ‘opening region’ and the area between walls and valves as ‘sinus region’ is for easier differentiation and discussion.

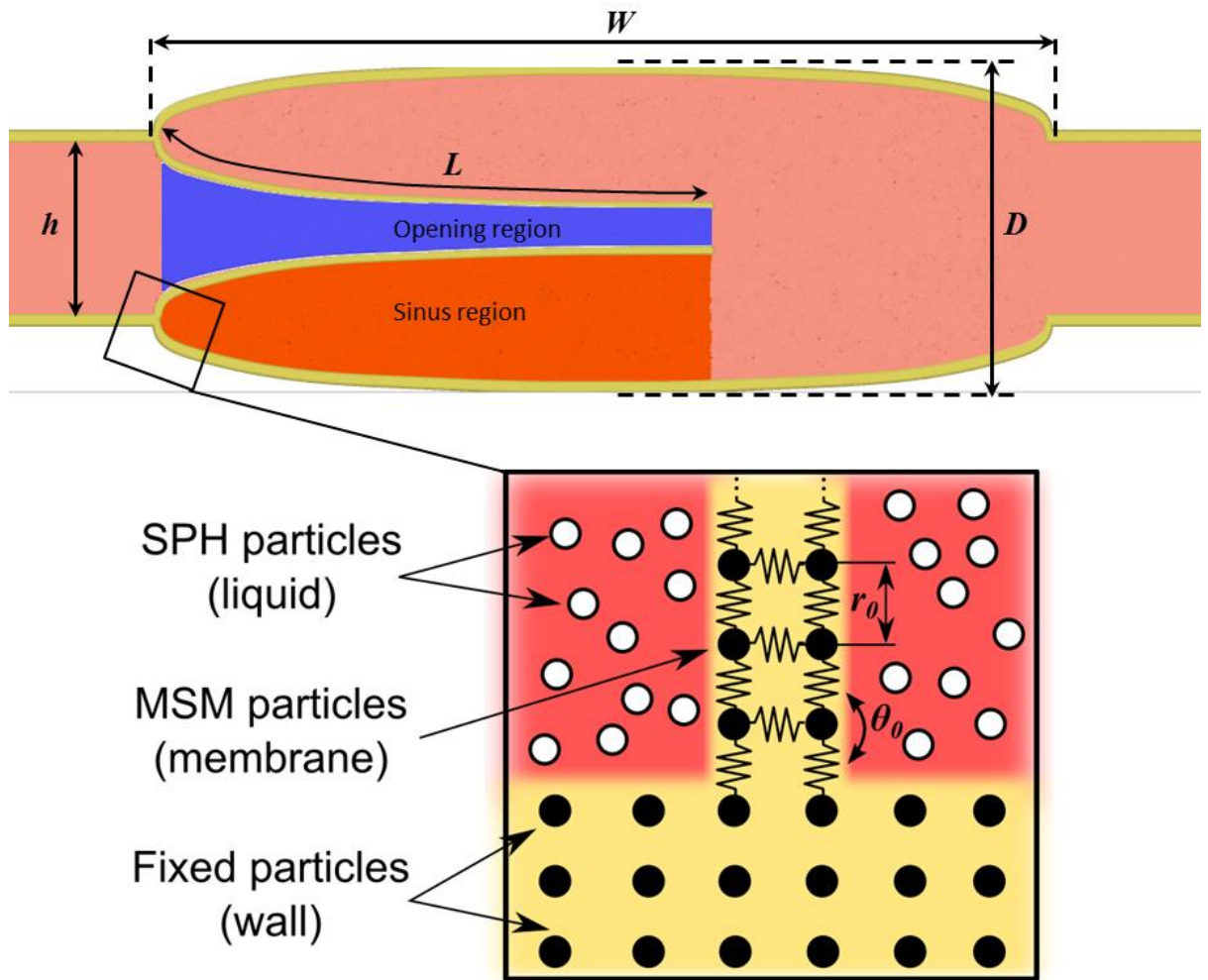


Figure. 4.2 Illustration of the venous valve 2D geometry and particle representation.

The geometry of model is represented by 95978 particles with an initial spacing distance 0.1mm. The fluid portion is represented only by SPH particles. In order to maximize the usage of this coupling method, the solid portion of model is treated with different method owing to their different physical character. The dynamic segment, namely, leaflets are symmetrically divided into (solid) MSM particles distributed in two layers respectively, with their connection built on springs and chains (Figure. 4.2). As for the stationary segment, SPH particles are adopted for the fixed walls distributed in three layers respectively.

4.3 Parameters for simulations in DMHS method

The computational springs and chains produces the Elastic modulus E and the flexural rigidity F of the venous valves, and detailed information for how the links are built up between them have been clearly explained later.

Similar to the treatment for Poiseuille flow and Couette flow, periodic boundary conditions are imposed on both the inlet and outlet. And a vascular pulsatile flow where only oscillation is taken into consideration is implemented by exerting acceleration on all liquid particles with amplitude g_0 given in table 4.1 and oscillation frequency $f = 1/T$ calculated from the reciprocal of oscillation period T . Compared to the in-vivo system, the computational load of model chosen here is greatly reduced by introducing a constant period and a simplified sinusoidal oscillation. In other words, the model is not set up as hydrodynamically equivalent to the real venous veins, however the model is chosen due to its balance between the accuracy and efficiency.

$$g = g_0 \sin(2\pi ft), \quad (4.1)$$

There is not clear reference in the literature for the actual flow velocities and oscillation frequencies in the venous valve. When the muscles contract the blood within the veins is squeezed in, the valve opens to promote the antegrade flow; when the muscles diastole, the valve closes to prevent the inverse flow. Because a high oscillation frequency cannot guarantee the complete closure of the valve, a sufficient period $T = 4s$ is chosen for the full closure. Simulation for each model is composed of 4 complete systole-diastole cycles.

Compared to previous studies (Wijeratne and Hoo 2008), this model has 1 more second for each cycle and 3 more cycles.

Generally speaking, the flow velocity is determined by the squeezing force of the muscles, which has the obviously positive correlation with the level of individual physical work.

For the sake of easier comparison, three peak inlet velocities used in the simulations: $0.03 \text{ m}\cdot\text{s}^{-1}$ (low physical velocity), $0.07 \text{ m}\cdot\text{s}^{-1}$ (intermediate case) and $0.13 \text{ m}\cdot\text{s}^{-1}$ (high level of physical velocity) respectively for different physical activity with three values of g_0 ($0.1 \text{ m}\cdot\text{s}^{-2}$, $0.25 \text{ m}\cdot\text{s}^{-2}$ and $0.4 \text{ m}\cdot\text{s}^{-2}$), while previous work only studied one activity level, Wijeratne and Hoo (2008) on the intermediate case and Simao et al. (2016) on low velocity case. Same as the actual physical condition, flows in all cases are laminar.

Besides, individual variation in length and flexibility of membrane also play vital role in determining the flow patterns. As shown in Table 4.1, three lengths (0.0256 m, 0.0175 m and 0.01 m) and three flexibilities (soft, normal and rigid membrane) are taken into consideration. The shortest membrane has the smallest size to ensure the full closure of the valves, while the longest size come from Wijeratne and Hoo (2008).

The length and the flexibility of membrane vary from person to person. In order to investigate a variety of individual variations, three membrane lengths are considered (0.0256 m, 0.0175 m and 0.01 m) and three flexibilities (soft, intermediate and rigid membrane, see Table 4.1).

Simulations	Length of the membrane L (m)	g_0 ($m \cdot s^{-2}$)	Angular coefficient k_a (J)	Type of the membrane
1	0.0256	0.1	0.01	Intermediate
2	0.0256	0.25	0.01	Intermediate
3	0.0256	0.4	0.01	Intermediate
4	0.01	0.1	0.01	Intermediate
5	0.01	0.25	0.01	Intermediate
6	0.01	0.4	0.01	Intermediate
8	0.0256	0.25	0.0001	Soft
19	0.0175	0.25	0.01	Intermediate
24	0.0175	0.1	0.01	Intermediate
25	0.0175	0.4	0.01	Intermediate
29	0.0256	0.25	0.005	Soft
30	0.0256	0.25	0.002	Soft
31	0.0256	0.25	0.02	Rigid
32	0.0256	0.25	0.05	Rigid

Table 4.1 Initial parameters list for fluid and membrane

The agglomeration algorithm was introduced to the cardiac valves by Ariane et al. (2017) where a thorough explanation of the approach was given. As mentioned above, since the dynamics of real venous blood transportation remains still unclear and the formation

mechanism of blood clots are too complex, The research effort has focused on the investigation of the main physical features in the flow in this chapter.

Some fluid particles are chosen as the seeds for the agglomeration, the list of agglomerate particles is updated per N time step by testing the particles within the distance R_{\max} around the seeds with a definite possibility of the solidification.

Owing to the limitation of computational power and requirements for efficiency, an accelerative process is developed for our agglomerate formation compared to the real cases. Although decrease the cycle number of the simulation, the reliability of our results is not reduced by adopting a larger time scale for agglomeration than the flow.

SPH (Equation. 2.8–2.22)	
Parameter	Value
Number of SPH wall particles (3 layers)	5360
Number of SPH valve particles (2 layers)	(1) 1026, (2) 702, (3) 402
Number of SPH fluid particles	(1) 89592, (2) 89726, (3) 90012
Mass of each particles (fluid)	$1.05 \cdot 10^{-5}$ kg
Mass of each particles (wall and valve)	$2 \cdot 10^{-5}$ kg
Initial distance among particles Δr	$1 \cdot 10^{-4}$ m
Smoothing length h	$2.5 \cdot 10^{-4}$ m
Artificial sound speed c_0	10 m s ⁻¹
Density ρ_0	1056 kg·m ⁻³
Time step Δt	10^{-7} s
CGMD (Equation.s 2.23–2.26)	
Parameter	Value
Angular coefficient k_a	See table 4.1
Hookian coefficient k_b	$1 \cdot 10^6$ J m ⁻²
Equilibrium distance r_0	$1 \cdot 10^{-4}$ m

Equilibrium angle Θ_0	$\pi/2$ rad
BOUNDARIES (eq. 2.30)	
Constant K	$4 \cdot 10^{-4}$ J
Repulsive radius r^*	$1 \cdot 10^{-4}$ m
CLOT FORMATION (Section Formation of solid aggregates)	
Number of time step for clot formation N	$0.5 \cdot 10^6$ s
R_{\max}	$2.5 \cdot 10^{-4}$ m
Agglomeration probability P	50 %
Max bonds per clot particle	4
(a) long, (b) medium, (c) short membrane	

Table 4.2 Specific parameters adopted for models and algorithm

4.4 Results and discussion

4.4.1 Force and velocity results

From the simulations, both the forces acting on computational particles and their velocities can be determined. The following discussion focuses in particular on the mechanical stress and the retention time, which are calculated, respectively, from the force and velocity data. These two factors are targeted because they are both related to thrombus formation. High mechanical stress brings to the activation of the platelets, while low retention times increase the probability that activated platelets aggregates (Zhang et al. 2002). In this subsection, a discussion is made of mechanical stress and retention time for a specific set of geometry and simulation conditions that is indicated as the “reference case” (long leaflets, low physical activity, and intermediate membrane). In Section 4.4.4, how mechanical stress and retention time change with the length of the leaflets is investigated, the intensity of physical work and the rigidity of the membrane.

4.4.2 Mechanical stress

In the literature, the main fluid variable usually linked to thrombus formation is shear stress (Zhang et al., 2002). Based on the simulation results, the calculated shear stress values are only significant in the opening region but insignificant in other regions. According to the medical experience, there exists a negative correlation of the formation of thrombus and the value of shear stress. That is to say, this cognition is coincident with simulations, thrombi is prone to aggregate in sinus regions rather than the opening region.

Recent studies (Ju et al. 2016) suggest that total mechanical stress rather than shear stress alone triggers blood agglomeration. This view seems consistent with simulations: Figure 4.3b shows that, while shear is only notable on the opening region, the total mechanical stress T_{tot} is high on both sides of the leaflets.

The total mechanical stress in our simulations is a combination form consists of the shear stress and pressure forces without the gravity taken into consideration. Therefore the value of T_{tot} is a two-factor cases which cannot be determined by only pressure term, as illustrated in Figure 4.3c. While calculations presented here are consistent with the findings of Ju et al. (2016), and suggest that the activation in the sinus region could depend on the overall mechanical stress rather than shear alone, high stresses do not automatically imply clot formation.

Compared to the single phase flow, transportation of solid-liquid mixture will produce an excess force termed as *added force*, which comes from the change of the relative velocity

of the solid portion with respect to the fluid and can give reasonable explanation for the stronger mechanical total stress in the sinus region.

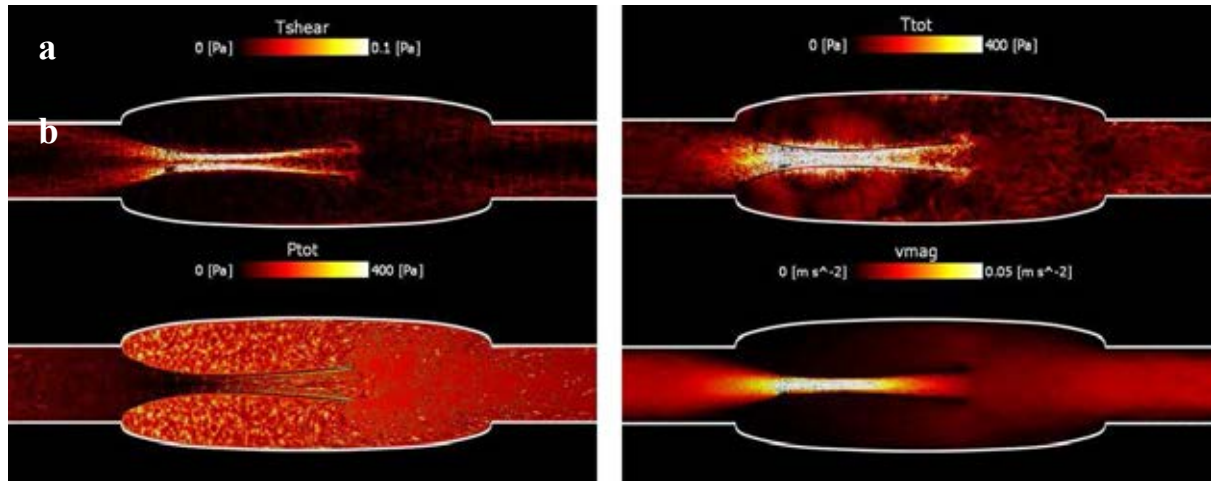


Figure. 4.3 Shear rate (a), total stress (b), pressure force (c), and velocity magnitude (d) for $L0.0256m/V0.03m\cdot s^{-1}/k_a0.01J$

If the local velocity is high, platelets move away from the area of high stress before they have time to aggregate (Zhang et al. 2002). If the velocity is low, the higher retention time increases the chances of aggregation. This would explain why thrombi were observed in the sinus region, but not in the opening region. Mechanical stress is high on both sides of the membrane (on the opening side is even higher), but only on the sinus side the velocity is low (Figure 4.3d).

Besides stress, therefore, another important parameter needs investigation is residence time.

4.4.3. Retention time in the sinus

Compared to Eulerian approach, displacement can be treated as the substitute of the retention time in Lagrangian method, so the displacement is used instead for convenience in this subsection.

As discussed in the previous section for Figure 4.3d, the velocity of particles in the sinus region is relatively low, as a result they required longer retention time compared to the opening region. Same conclusion can be obtained again through Figure 4.4. Particles in sinus regions are labelled in blue from the initial zero displacement state and their instantaneous location is recorded every one cycle. After 4 cycles, particles initially in the sinus region partially leave with a relatively high speed and most of them are marked in red, however others with lower velocity have shorter displacement. Two regions can be recognized as the high-displacement zone. First one is circled and marked as the ‘mixing region’ near the sinus wall and is consistent with the reverse flow area generated by the regressive flow. Another one is termed as ‘compression region’ near the membrane and moves coincidentally with the motion of the membrane. Nevertheless two regions have different driving mechanism for particles. While the particles in mixing region are carried out of the sinus by the backflow, particles from compression region are passively cast off by the to-and-fro oscillation of the membrane.

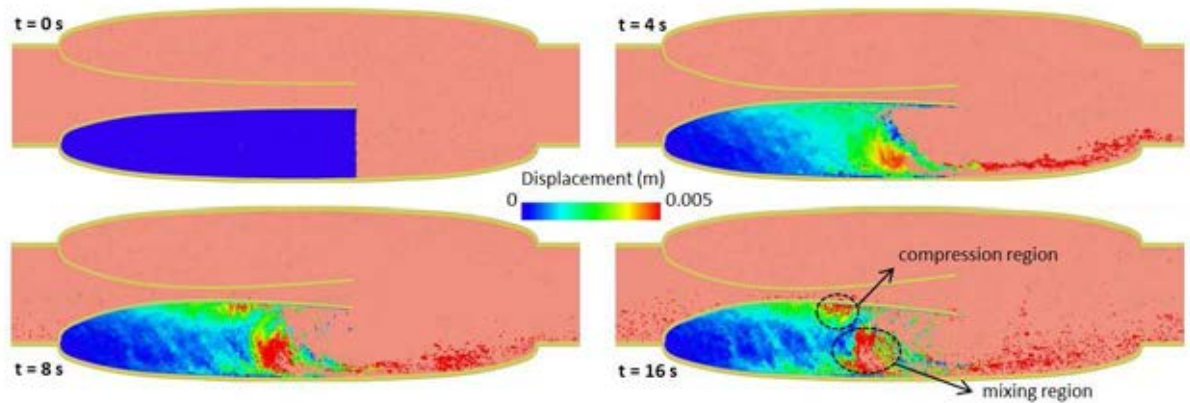


Figure. 4.4 Snapshots taken every cycle of initial sinus fluid particles marked with color-coded displacement for $L=0.0256\text{m}/V=0.03\text{m}\cdot\text{s}^{-1}/k_a=0.01\text{J}\sim 0.05\text{J}$

From the agglomeration perspective, this makes a considerable difference because residence time is much lower in the mixing region. On that basis the displacement is the imperfect substitution of the retention time, a more accurate alternative will be shown in the following parametric study for the improvement.

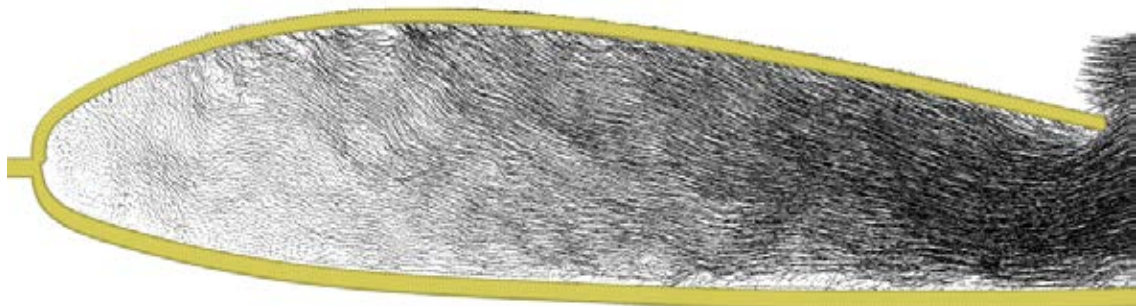


Figure. 4.5 Velocity profile in the sinus area (vectors).

4.4.4 Parametric study

Investigation is made into the following parameters, namely, membrane flexibility and its length, flow velocity will exert impact on the mechanical total stress and displacement in this subsection.

On the basis of simulations shown here, in fact, all the three factors are extremely important for the function of the valve. However, as the parameters for each simulations are space-time variables, the comparisons will not be intuitive. Concerning space, particle in the sinus region below the membrane with maximum total stress is recognized for each simulation and the comparisons is implemented among them. In this way, the measurement is made at relatively identical location. At this location, neither the total stress nor the displacement remains unchanged (Figure 4.6a and 4.6b). As for the displacement, a time-average term is adopted to replace the instantaneous one for further discussion. Concerning the total stress, the maximum stress is preferred because this is what promotes agglomeration more than their average.

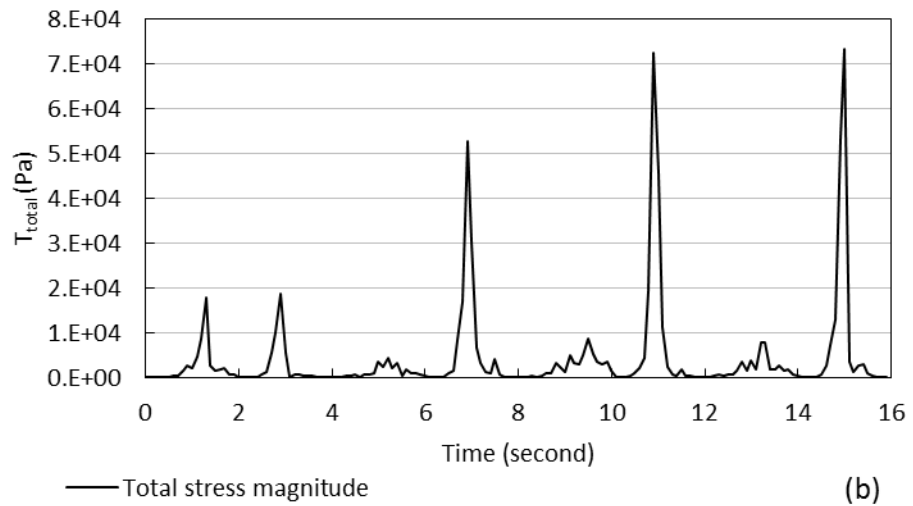
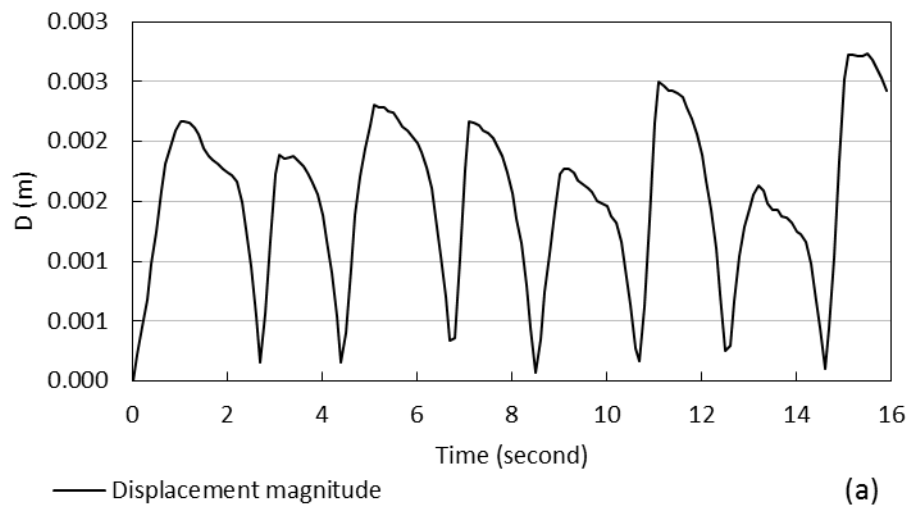


Figure. 4.6 Evolution of displacement (a) and peak total stress magnitude (b)

with time for $L=0.0256\text{m}/V=0.03 \text{ m}\cdot\text{s}^{-1}/k_a=0.01\text{J}$

The oscillation with time of both parameters are quantified by their standard deviations. As shown in the following subsection, the error bars measure the fluctuation of the displacement (Figure 4.7a). However, for the total stress, they measure the deviation of the peak force for each cycle (Figure 4.7b).

4.4.4.1. Effect of membrane rigidity

In Figure 4.7, both displacement and total stress continuously decrease until $k_a = 0.02$ J because membrane deforms less owing to the low flexibility. Nevertheless the displacement has a bounce for the most rigid membrane with $k_a = 0.05$ J. Comparisons between top two snapshots in Figure 4.8 at $k_a = 0.05$ J can give reasonable explanation for this phenomenon. During the membrane closure time, the contour of the membrane is straight type for the intermediate rigidity ($k_a=0.01$ J) in Figure 4.8a. However the rigid membrane with $k_a=0.05$ J bends towards the sinus region driven by the reverse flow. Consequently the reverse flow can be partly prevented by the shrunk path to the sinus region and displacement is smaller owing to the decelerated particles. Contrarily irregular large deformation can be observed in the membrane with excess flexibility ($k_a=0.0001$ J), the membrane cannot hold back the reverse flow and even swings with the flow.

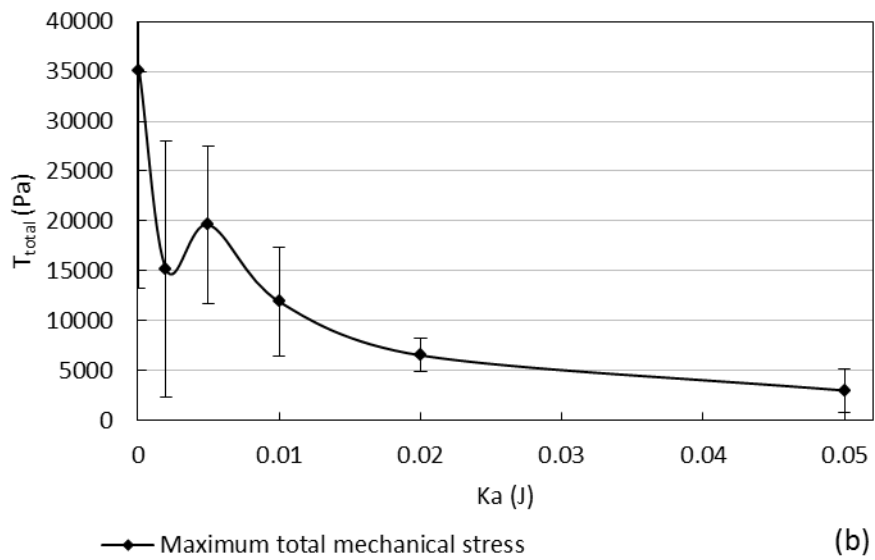
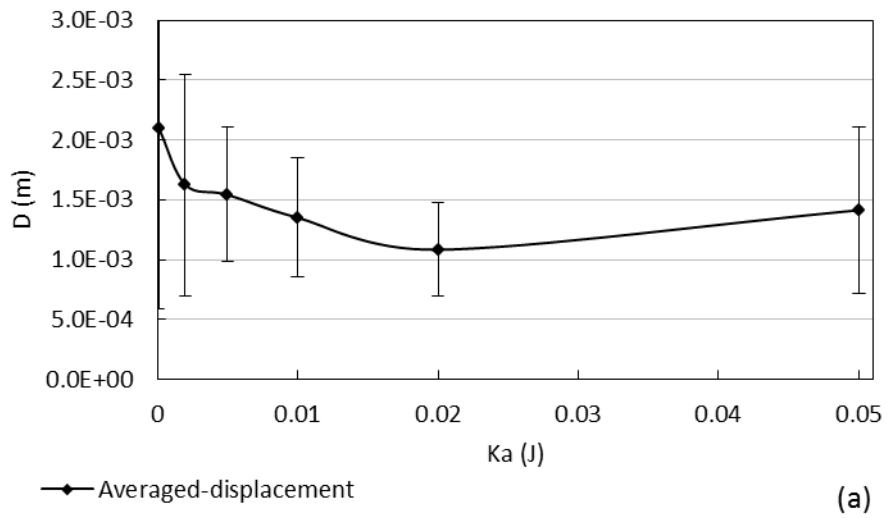


Figure. 4.7 Evolution of averaged-displacement (a) and total mechanical stress (b) with the valve flexibility for simulations operated with $L=0.0256\text{m}/V=0.03 \text{ m}\cdot\text{s}^{-1}$

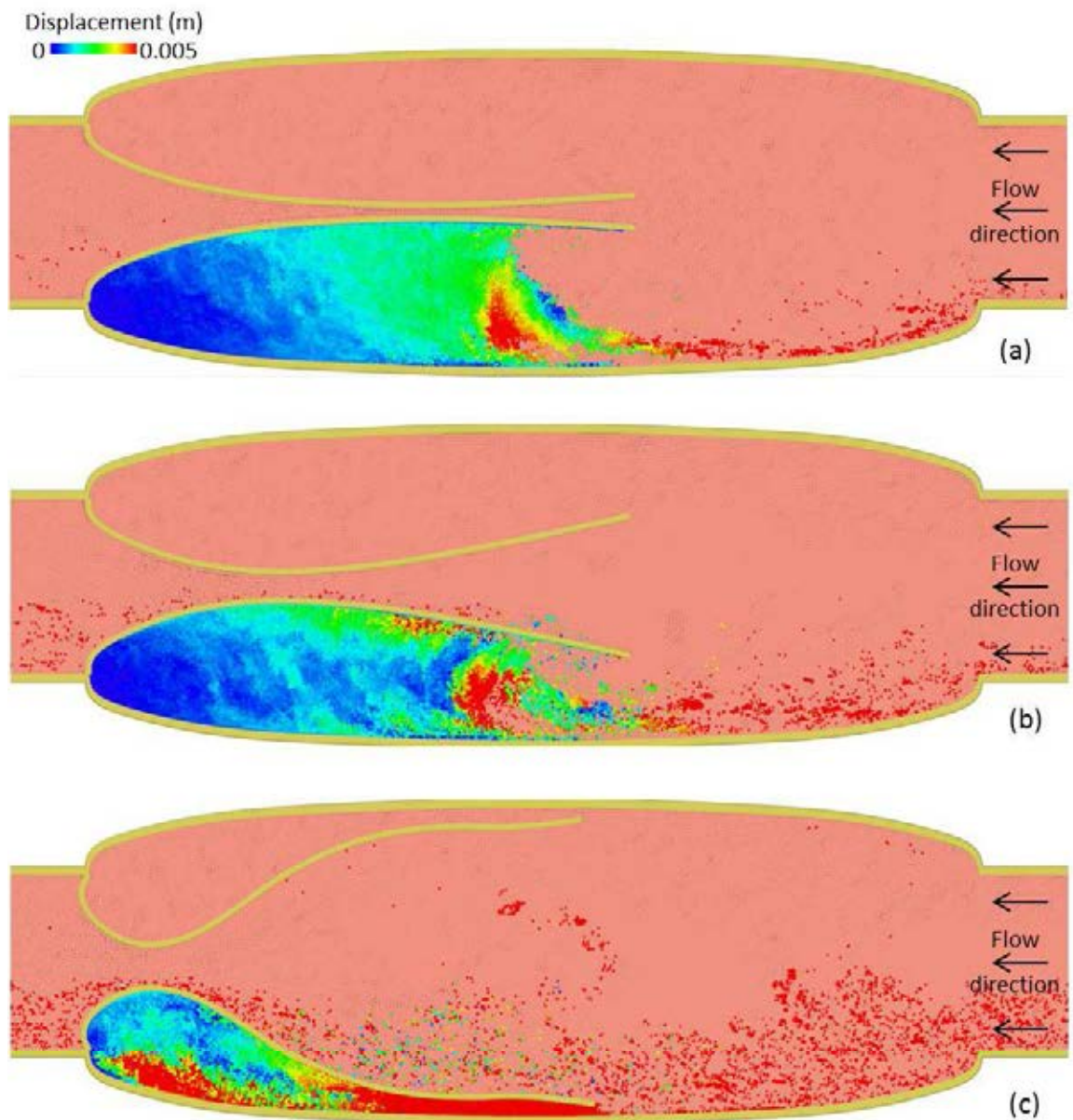
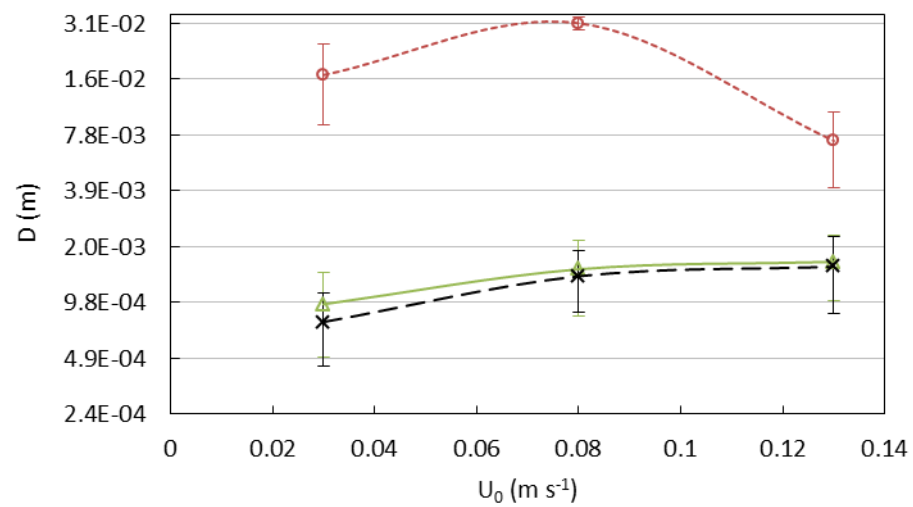


Figure. 4.8 Snapshots for the fluid movement of the initial sinus fluid particles marked with color-coded displacement of simulations for $L=0.0256\text{m}/V=0.07\text{ m}\cdot\text{s}^{-1}$ for $k_a = 0.01\text{ J}$ (a), $k_a = 0.05\text{ J}$ (b), and $k_a = 0.0001\text{ J}$

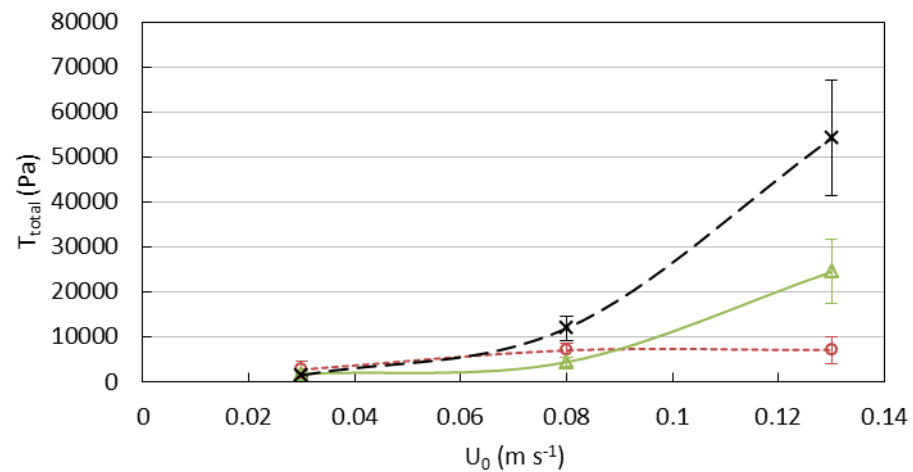
4.4.4.2 Effect of membrane length and inlet velocity

Figure 4.9 illustrates how the inlet velocity influences the displacement and total stress at three membrane lengths. Same as expectation, total stress and displacement has an obviously positive correlation with velocity in two longer membrane. Differently, for the

shortest length, both the stress and displacement reaches their peak more quickly, Figure 4.10 gives the explanation: the stress peak generates in the intermediate section instead of the membrane tip. Accordingly, fluid particles moves more easily affected by the hemodynamic in the opening region. As a result, they suffer less impediment and a smoother flow is obtained, resulting in a significant rise in the displacement.



Averaged-displacement : ---○--- short —△— medium —×— long (a)



Maximum total mechanical stress : ---○--- short —△— medium —×— long (b)

Figure. 4.9 Evolution of displacement (a) and total stress magnitude (b) with the maximum inlet velocity.

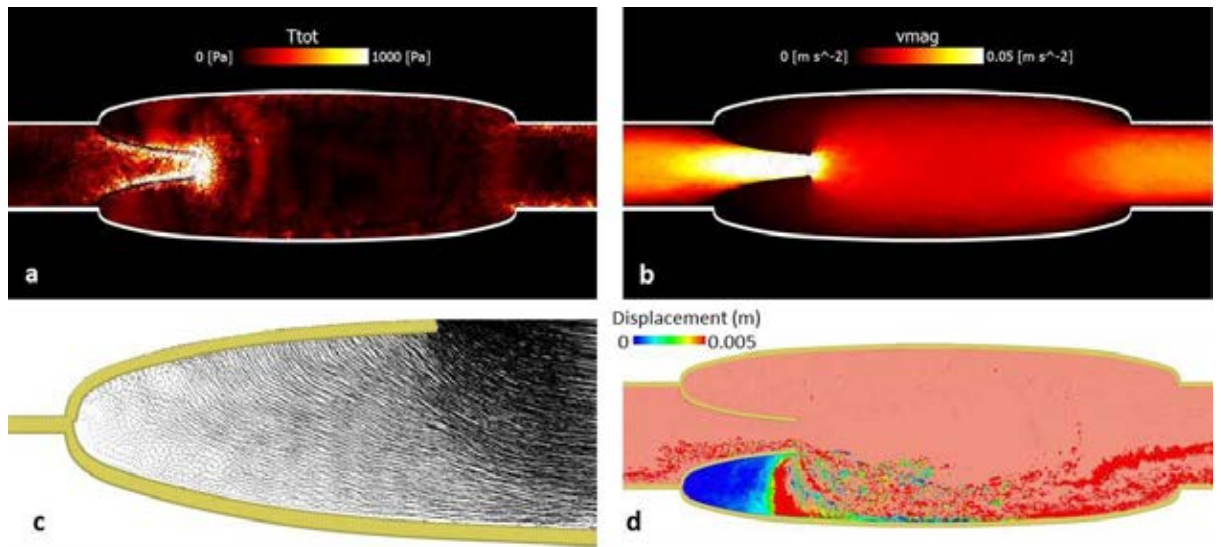


Figure. 4.10 Total stress (a), velocity magnitude (b), velocity vector (c), and displacement (d) for simulations operated with $L=0.01\text{m}/V=0.07\text{m}\cdot\text{s}^{-1}/k_a=0.01\text{J}$.

4.5. Agglomeration

As mentioned in last section, the agglomeration algorithm can help to explain the aggregation of blood clotting from physical perspective. As the agglomeration is a complicated phenomenon caused by multiple factors, not all the overall causes and entire process can be accounted for, simulations only focused on the physical dynamics are adopted to approximate the real conditions.

Retention time and total stress are the two major elements influence upon the agglomeration. The two crucial positions where they reaches their peak values independently become the research focus. As shown in Figure 4.11, P_1 is for the peak stress and located at the sinus region near the middle of the membrane, P_2 is for the maximum retention time and located between the membrane and the venous wall. Points

are chosen as the seeds for the agglomeration algorithm, so the agglomeration list starts from them and the algorithm is adopted for periodic update to renew the list.

Relevant parameters have been given in Table 4.2 for the upcoming simulations. Time scale is much shorter compared to the real blood clotting formation as we want to foster the development of the thrombi in fewer cycles.

Though the particles are pushed towards the peak stress point P_1 and the number of potential particles for the blood clotting area with radius R_{MAX} and center P_1 increases, they move too fast to have sufficient retention time for the thrombi formation. Conversely, another seed has smaller stress and velocity, so the clotting is more easily to form in its affected area.

Both high stresses and long retention time can promote the formation of aggregation. By comparison in Figure 4.11, it reveals that the retention time plays a more crucial role in the thrombi accumulation than the stress.

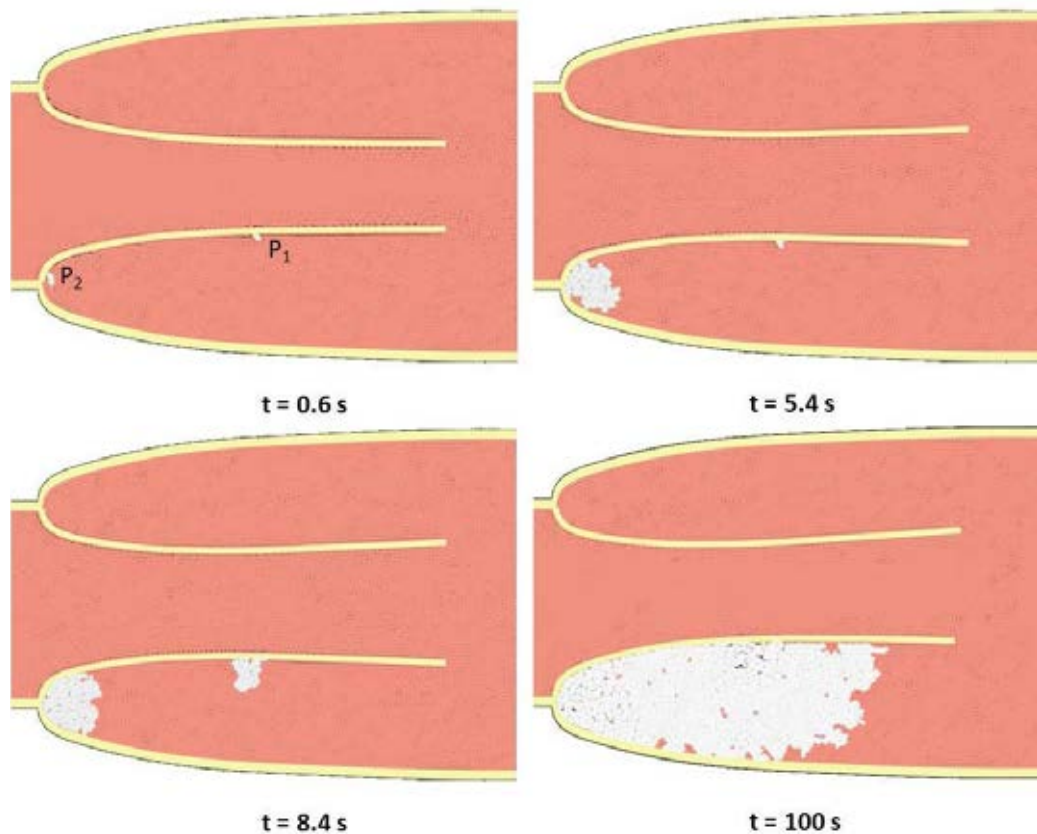


Figure. 4.11 Solid aggregates in the sinus region at different times for
 $L=0.0175\text{m}/V=0.07\text{m}\cdot\text{s}^{-1}/k_a=0.01\text{J}$.

4.6 Conclusions

This chapter adopts a discrete multi-physics models to investigate the hemodynamic and flap mechanics develops in lower limb veins. The formation of thrombi is described in two parts: firstly the key parameters are investigated to explain how certain total mechanical stress and adequate retention time will create conditions for the blood clotting. Then the process of blood congealing, clot formatting and thrombus aggregating is implemented by adding the agglomeration algorithm to the simulation process.

As for the initial model parameters, the flexibility and size of the membrane have a significant influence on both the stress and retention time. Strong rigidity might fail to

block the reverse flow sufficiently owing to the incomplete closure of the membrane. Nevertheless, the excess backflow creates the recirculation within the sinus region, which can partially sweep away the potential stagnated content and reduce the risk of clot formation. Likewise, short membrane also benefit from less clot aggregation reduced by smaller sinus region.

Comparison is made between stress and retention time by implanting two thrombi seeds, and the level of their growth shows that the stress has a higher effect upon the development of blood clotting. The function of retention time is emphasized owing to the relatively low velocity in veins and can be more harm for the functional veins.

The investigation into the venous valves not only reconfirms the known cognition that the flexibility and size of membrane will have influence on the clot formation, but also stresses the significant role of individualized diagnosis for future individualized treatment. Nowadays, CT scan has been widely used to capture the precise geometry of the venous valve of a particular individual. However, usually the given information is insufficient for the diagnosis and no prediction can be made to tell possibility of DVT. Therefore models presented here can be adopted as a new powerful aid in helping with the personalized diagnosis by means of building up more accurate models to simulate, analyze and predict the particular cases.

Chapter 5

Conclusions and Future Work

5.1 Conclusions

Complicated characteristics of biological flows within different body parts have drawn great attention and massive investigation implemented by CFD modelling. Compared to the experimental and clinical approaches, CFD stands out as a powerful and trustworthy tool that has obvious strengths in simulations for a variety applications. It has advantage of expense-saving, flexible operation and reliable outcomes. However as for the biological flows, though the traditional method can utilize non-invasive diagnosis measurements and propose models for microscale tissues that cannot be detected by current techniques, owing to the complex mechanism of the real conditions and the disadvantage of the conventional mesh methods, most of the models appear to be oversimplified or ineffective. Different from the grid-based approaches, mesh-free Lagrangian style method has great potential to develop more accurate biological models with less computational power consumption. In this thesis, investigations are made into two different multi-phase transportation phenomena.

5.1.1 Modelling of intestine segments by DMHS method

Stands out as a time-saving, cost-saving, easy-to-operate and manageable approach, CFD is gaining its popularity in building up models for intestine, and a large number of investigations

have been made into study the mechanism of the food transportation inside it. However most previous studies lacks of the flexible walls and thus the peristalsis cannot be satisfied. A model is proposed that can achieve this goal. The intestine membrane is flexible and its periodic peristalsis conveys food along the boundary tissues. Another emphasis of models is the partially-filled model to approximate the general intestine conditions to the most extent. Results are validated by experimental outcomes and the model is already adopted for practical applications. Investigation into the hydrodynamics develops in the large intestine not only deepen our understanding of the in-vitro models but also improve the experimental skills.

Only a small haustra segments is needed in the experiment to measure α for our models. The flow front propagates with a marching velocity u_F , which can be determined by the measured α and u_P calculated by Reynolds number.

As mentioned before, less intestine pockets are needed for the experiments as most of them can be treated equally, but the exception to that is the first pocket. As a result, in order to reduce measuring errors, tracer particles will not be rejected into the first segment in our PET-style experiments.

5.1.1 Modelling of venous valves by DMHS method

Same approach is adopted for investigation into leg venous valve models of the fluid dynamics incorporate with membrane characteristics. The illustration of clot formation is comprised of two

parts: precondition and coagulation. Essential properties, total stress and retention is recognized as the key factors to create proper environment for initial clot formation and then the clot starts to aggregate. The simulations of aggregation process are implemented by the agglomeration algorithm. The two key parameters for aggregation are determined by the initial model properties. For instance, the flexibility of the membrane can exert considerable influence on the backflow pattern. When it is strongly rigid, the efficiency of preventing the reverse flows might be reduced owing to the gap between the flaps. However it creates a stronger recirculation that may carry the stagnation away from the sinus region. As for the size of the membrane, the shorter membranes are less risky in developing clots as long as their length can guarantee a complete closure.

Comparison between the stress and residence time illustrates that the dominant factor is the residence time. Two planted clot seeds for peak stress and residence time have shown that even the aggregation is greatly affected by the stress, the particles with longer residence time will be stagnated with much more possibility with the low speed of the venous flows.

Specific models for individuals can be proposed for a good option for the diagnosis and prediction. Compared to other techniques can provide certain information, the mature and accurate models can offer more precise data for a supplement or even for the substitute for the diagnosis and prediction.

5.2 Future recommendations

In this work, the capability of DMHS method for modelling the biological fluid is discussed in detail. The validation of the simulation results is completed by comparison with the experimental data or the previous literatures. Both the strengths and weakness of this approach are illustrated.

As for intestine modelling, a mathematical model is developed to describe the transportation of the viscous fluids within the partially filled intestine with periodic peristalsis. Models are validated against the experimental data. Two mass transportation mechanisms are identified by the model, revealing that the pouring mode is more dominant for its greater mixing effect while the surfing mode moves faster with less mixing. A series of measures are proposed to increase the reliability of in-vitro models based upon the obtained cognition. Tracers for measurement can be injected into every pocket except the first one. In this work, only the injection position is studied, obviously other characteristics of tracers can also have great influence on the fluid pattern. For instance, part of the future work can focus on the hydrodynamics influenced by the tracer viscosity. Or the food content can be further complicated by introducing solid segments even with the agglomeration, fragmentation and mixing with the viscous fluid content.

Besides the DMHS method, investigation into models designed for venous valves also involves in the agglomeration algorithm to give illustration for the clot formation. The retention time is proven to play a more significant role in influencing the thrombus agglomeration in veins. In addition, the over-rigid membrane and short leaflets will induce an ineffective blood

transportation. However owing to the greater reflux content in sinus region is a more complete mixing is generated, which can reduce the possibility for the clot formation. Though a lot of improvement for models has been made compared to the previous studies, there are yet still many vacuum to be filled in simulations presented here. For instance, future work can be related to the more complicated flows consist of other modelling subjects (i.e. the blood cells) with biological process (i.e. the blood coagulation promoted by enzyme). Combined with agglomerated seeds added for the agglomeration algorithm, this updated content will improve the reliability of models at present.

Reference

Agertz, O., Moore, B., Stadel, J., Potter, D., Miniati, F., Read, J, Pearce, F. (2007). Fundamental differences between SPH and grid methods. *Monthly Notices of the Royal Astronomical Society*, 380(3), 963-978.

Aguiar, C. E., Hama, Y., Kodama, T., Osada, T. (2001). Event-by-event fluctuations in hydrodynamical description of heavy-ion collisions. arXiv preprint hep-ph/0106266.

Akbar, N. S.,Nadeem, S. (2014). Simulation of peristaltic flow of chyme in small intestine for couple stress fluid. *Meccanica*, 49(2), 325-334.

Alexiadis A. (2014) A smoothed particle hydrodynamics and coarse-grained molecular dynamics hybrid technique for modelling elastic particles and breakable capsules under various flow conditions. *Int J Num Meth Eng*; 100:713–719.

Alexiadis A., (2015a) The Discrete Multi-Hybrid System for the simulation of solid-liquid flows *PLoS ONE* 10(5): e0124678

Alexiadis A. (2015b) A new framework for modelling the dynamics and the breakage of capsules, vesicles and cells in fluid flow, *Procedia UTAM* 16:80-88.

Alexiadis A., Lockerby D.A., Borg M.K. and Reese J.M. (2013), A Laplacian-based algorithm for non-isothermal atomistic-continuum hybrid simulation of micro and nano-flows, *Computer Methods in Applied Mechanics and Engineering*, 264:81-94

Alexiadis A., Lockerby D.A., Borg M.K. and Reese J.M. (2014), The atomistic-continuum hybrid taxonomy and the hybrid-hybrid approach, *International Journal for Numerical Methods in Engineering* 98: 534-546

Alexiadis A., Lockerby D.A., Borg M.K. and Reese J.M. (2015) A particle-continuum hybrid framework for transport phenomena and chemical reactions in multi-component systems at the micro and nano-scale *Journal of Heat Transfer* 137: HT-14-1130

Al-Saad, M. (2017). Blood flow simulation using smooth particle hydrodynamics (Doctoral dissertation, Cardiff University). URI: <http://orca.cf.ac.uk/id/eprint/104316>

Altomare, C., Crespo, A. J., Domínguez, J. M., Gómez-Gesteira, M., Suzuki, T., Verwaest, T. (2015). Applicability of Smoothed Particle Hydrodynamics for estimation of sea wave impact on coastal structures. *Coastal Engineering*, 96, 1-12.

Ariane M., Allouche H., Bussone M., Giacosa F., Bernard F., Alexiadis A. (2016) Hybrid SPH modelling of an aortic valve with flexible leaflets, submitted to *Journal of Biomechanics*.

Ariane, M., Allouche, M. H., Bussone, M., Giacosa, F., Bernard, F., Barigou, M., Alexiadis, A. (2017). Discrete multi-physics: A mesh-free model of blood flow in flexible biological valve including solid aggregate formation. *PloS one*, 12(4), e0174795.

Batchelor, G. K., Young, A. D. (1968). An introduction to fluid mechanics. *Journal of Applied Mechanics*, 35, 624.

Bavo, A. M., Rocatello, G., Iannaccone, F., Degroote, J., Vierendeels, J., Segers, P. (2016). Fluid-structure interaction simulation of prosthetic aortic valves: comparison between immersed boundary and arbitrary Lagrangian-Eulerian techniques for the mesh representation. *PloS one*, 11(4), e0154517.

Becker, M., Teschner, M. (2007, August). Weakly compressible SPH for free surface flows. In *Proceedings of the 2007 ACM SIGGRAPH/Eurographics symposium on Computer animation* (pp. 209-217). Eurographics Association.

Benz, W., Asphaug, E. (1995). Simulations of brittle solids using smooth particle hydrodynamics. *Computer physics communications*, 87(1), 253-265.

Birdsall, C. K. (1991). Particle-in-cell charged-particle simulations, plus Monte Carlo collisions with neutral atoms, PIC-MCC. *IEEE Transactions on Plasma Science*, 19(2), 65-85.

Bonet, J., Kulasegaram, S. (2000). Correction and stabilization of smooth particle hydrodynamics methods with applications in metal forming simulations. *International journal for numerical methods in engineering*, 47(6), 1189-1214.

Borazjani, I. (2015). A review of fluid-structure interaction simulations of prosthetic heart valves. *Journal of long-term effects of medical implants*, 25(1-2).

Bovill, E. G., van der Vliet, A. (2011). Venous valvular stasis–associated hypoxia and thrombosis: what is the link? *Annual review of physiology*, 73, 527-545.

Bradshaw, P. (2016). *Experimental Fluid Mechanics: Thermodynamics and Fluid Mechanics Division*. Elsevier.

Brill, A., Fuchs, T. A., Chauhan, A. K., Yang, J. J., De Meyer, S. F., Köllnberger, M., Wagner, D. D. (2011). von Willebrand factor-mediated platelet adhesion is critical for deep vein thrombosis in mouse models. *Blood*, 117(4), 1400-1407.

Broadbent, C. J., Bridgwater, J., Parker, D. J., Keningley, S. T., and Knight, P. (1993). A phenomenological study of a batch mixer using a positron camera. *Powder Technology*, 76(3), 317-329.

Buxton, G. A., Clarke, N. (2006). Computational phlebology: the simulation of a vein valve. *Journal of biological physics*, 32(6), 507-521.

Cleary, P. W., Monaghan, J. J. (1999). Conduction modelling using smoothed particle hydrodynamics. *Journal of Computational Physics*, 148(1), 227-264.

Cleary, P. W., Cohen, R. C., Harrison, S. M., Sinnott, M. D., Prakash, M., Mead, S. (2013). Prediction of industrial, biophysical and extreme geophysical flows using particle methods. *Engineering Computations*, 30(2), 157-196.

Crosetto, P., Deparis, S., Quarteroni, A., Stergiopoulos, N. (2013). Physiological simulation of blood flow in the aorta: comparison of hemodynamic indices as predicted by 3-D FSI, 3-D rigid wall and 1-D models. *Medical engineering & physics*, 35(6), 784-791.

Dinning, P. G., Wiklendt, L., Maslen, L., Gibbins, I., Patton, V., Arkwright, J. W., Lubowski, D. Z., O'Grady, G., Bampton, P. A., Brookes, S. J., and Costa, M. (2014). Quantification of in vivo colonic motor patterns in healthy humans before and after a meal revealed by high-resolution fiber-optic manometry. *Neurogastroenterol Motil*, 26(10), 1443-1457.

Dolag, K., Vazza, F., Brunetti, G., Tormen, G. (2005). Turbulent gas motions in galaxy cluster simulations: the role of smoothed particle hydrodynamics viscosity. *Monthly Notices of the Royal Astronomical Society*, 364(3), 753-772.

Ebeling, W., Schweitzer, F. (2002). Self-organization, active brownian dynamics, and biological applications. arXiv preprint cond-mat/0211606.

Fenlon, A. J., David, T. (2001). Numerical Models for the Simulation of Flexible Artificial Heart Valves: Part I-Computational Methods. *Computer methods in biomechanics and biomedical engineering*, 4(4), 323-339.

Ferrari, A. (2010). SPH simulation of free surface flow over a sharp-crested weir. *Advances in Water Resources*, 33(3), 270-276.

Ferrua, M. J., Singh, R. P. (2015). Computational modelling of gastric digestion: current challenges and future directions. *Current Opinion in Food Science*, 4, 116-123.

Frank, A. O., Walsh, P. W., Moore, J. E. (2002). Computational fluid dynamics and stent design. *Artificial organs*, 26(7), 614-621.

Gingold, R. A., Monaghan, J. J. (1977). Smoothed particle hydrodynamics: theory and application to non-spherical stars. *Monthly notices of the royal astronomical society*, 181(3), 375-389.

Guerra, A., Etienne-Mesmin, L., Livrelli, V., Denis, S., Blanquet-Diot, S., Alric, M. (2012). Relevance and challenges in modeling human gastric and small intestinal digestion. *Trends in biotechnology*, 30:591–600.

Halevi, R., Hamdan, A., Marom, G., Mega, M., Raanani, E., Haj-Ali, R. (2015). Progressive aortic valve calcification: Three-dimensional visualization and biomechanical analysis. *Journal of biomechanics*, 48(3), 489-497.

Helmholtz, H. V. (1845). Ueber den Stoffverbrauch bei der Muskelaktion.

Huang, Y., Zhang, W., Xu, Q., Xie, P., Hao, L. (2012). Run-out analysis of flow-like landslides triggered by the Ms 8.0 2008 Wenchuan earthquake using smoothed particle hydrodynamics. *Landslides*, 9(2), 275-283

Hunt, B. J. (2009). The prevention of hospital - acquired venous thromboembolism in the United Kingdom. *British journal of haematology*, 144(5), 642-652.

Hur, S. J., Lim, B. O., Decker, E. A., McClements, D. J. (2011). In vitro human digestion models for food applications. *Food Chemistry*, 125:1–12.

Jin, Q., Zhang, X., Li, X., Wang, J. (2010). Dynamics analysis of bladder-urethra system based on CFD. *Frontiers of Mechanical Engineering in China*, 5(3), 336-340.

Johnson, G. R., Stryk, R. A., Beissel, S. R. (1996). SPH for high velocity impact computations. *Computer methods in applied mechanics and engineering*, 139(1-4), 347-373.

Ju, L., Chen, Y., Xue, L., Du, X., Zhu, C. (2016). Cooperative unfolding of distinctive mechanoreceptor domains transduces force into signals. *Elife*, 5, e15447.

Kamensky, D., Hsu, M. C., Schillinger, D., Evans, J. A., Aggarwal, A., Bazilevs, Y., Hughes, T. J. (2015). An immersed-geometric variational framework for fluid–structure interaction: Application to bioprosthetic heart valves. *Computer methods in applied mechanics and engineering*, 284, 1005-1053.

Keener, J. P., Sneyd, J. (1998). *Mathematical physiology* (Vol. 1). New York: Springer.

Kozu, H., Kobayashi, I., Nakajima, M., Uemura, K., Sato, S., Ichikawa, S. (2010). Analysis of flow phenomena in gastric contents induced by human gastric peristalsis using CFD. *Food Biophysics*, 5(4), 330-336.

Krištof, P., Beneš, B., Křivánek, J., Št'ava, O. (2009, April). Hydraulic erosion using smoothed particle hydrodynamics. In *Computer Graphics Forum* (Vol. 28, No. 2, pp. 219-228). Blackwell Publishing Ltd.

Kyrle, P. A., Eichinger, S. (2005). Deep vein thrombosis. *The Lancet*, 365(9465), 1163-1174.

LaDisa, J. F., Olson, L. E., Guler, I., Hettrick, D. A., Audi, S. H., Kersten, J. R., Warltier, D.C., Pagel, P. S. (2004). Stent design properties and deployment ratio influence indexes

of wall shear stress: a three-dimensional computational fluid dynamics investigation within a normal artery. *Journal of Applied Physiology*, 97(1), 424-430.

Lanzafame, G. (2003). Spiral and shock front development in accretion discs in close binaries:

Lipinski, D., Mohseni, K. (2010, August). Cooperative control of a team of unmanned vehicles using smoothed particle hydrodynamics. In *Proceedings of the 2010 AIAA Guidance, Navigation, and Control Conference*, Toronto.

Liu GR, Liu MB. (2003) *Smoothed Particle Hydrodynamics: A Meshfree Particle Method*. Singapore: World Scientific Publishing.

Liu, M. B., Liu, G. R., Zong, Z., Lam, K. Y. (2003). Computer simulation of high explosive explosion using smoothed particle hydrodynamics methodology. *Computers & Fluids*, 32(3), 305-322.

Lucy, L. B. (1977). A numerical approach to the testing of the fission hypothesis. *The astronomical journal*, 82, 1013-1024.

Marom, G. (2015). Numerical methods for fluid–structure interaction models of aortic valves. *Archives of Computational Methods in Engineering*, 22(4), 595-620.

McQueen, D. M., Peskin, C. S. (2000). A three-dimensional computer model of the human heart for studying cardiac fluid dynamics. *ACM SIGGRAPH Computer Graphics*, 34(1), 56-60.

- Miandehi, E. E., M. H. Aazami, H. Niazmand, Y. Mesri, A. Deyranlou, and S. Eslami. 2015. Clinical simulation of aortic valve: a narrative review. *Studies in health technology and informatics* 210: 612-616.
- Misra J.C., Pandey S.K. (2006) Peristaltic transport of physiological fluids, J.C. Misra (Ed.), *Biomathematics: Modeling and Simulation*, World Scientific (2006), pp. 177–189
- Monaghan, J. J. 1992. Smoothed Particle Hydrodynamics. *Annual Review of Astronomy and Astrophysics* 30: 543-574.
- Monaghan, J. J. (1994). Simulating free surface flows with SPH. *Journal of computational physics*, 110(2), 399-406.
- Monaghan, J. J., Gingold, R. A. (1983). Shock simulation by the particle method SPH. *Journal of computational physics*, 52(2), 374-389.
- Monaghan, J. J., Kos, A. (1999). Solitary waves on a Cretan beach. *Journal of waterway, port, coastal, and ocean engineering*, 125(3), 145-155.
- Monaghan, J. J., Lattanzio, J. C. (1985). A refined particle method for astrophysical problems. *Astronomy and astrophysics*, 149, 135-143.
- Morbiducci, U., Ponzini, R., Gallo, D., Bignardi, C., Rizzo, G. (2013). Inflow boundary conditions for image-based computational hemodynamics: impact of idealized versus measured velocity profiles in the human aorta. *Journal of biomechanics*, 46(1), 102-109.

Morbiducci, U., R. Ponzini, D. Gallo, C. Bignardi, and G. Rizzo.(2013). Inflow boundary conditions for image-based computational hemodynamics: Impact of idealized versus measured velocity profiles in the human aorta. *Journal of Biomechanics* 46: 102-109.

Morris JP, Fox PJ, Zhu Y. (1997) Modeling Low Reynolds Incompressible Flows Using SPH. *J Comput Phys*; 136:214–226.

Müller M, Schirm S, Teschner M, Heidelberger B, Gross M. (2004) Interaction of fluids with deformable solids. *Comp Animat Virt W*; 15:159–171

Mylavarapu, G., Murugappan, S., Mihaescu, M., Kalra, M., Khosla, S., Gutmark, E. (2009). Validation of computational fluid dynamics methodology used for human upper airway flow simulations. *Journal of biomechanics*,42(10), 1553-1559.

Neal, M. L., Kerckhoffs, R. (2009). Current progress in patient-specific modeling. *Briefings in bioinformatics*, bbp049.

Nelson, D., Vogelsberger, M., Genel, S., Sijacki, D., Kereš, D., Springel, V., Hernquist, L. (2013). Moving mesh cosmology: tracing cosmological gas accretion. *Monthly Notices of the Royal Astronomical Society*, sts595.

Pal, A., Indireskumar, K., Schwizer, W., Abrahamsson, B., Fried, M., Brasseur, J. G. (2004). Gastric flow and mixing studied using computer simulation. *Proceedings of the Royal Society of London B: Biological Sciences*, 271(1557), 2587-2594.

Palyanov, A., Khayrulin, S., Larson, S. D. (2016). Application of smoothed particle hydrodynamics to modeling mechanisms of biological tissue. *Advances in Engineering Software*, 98, 1-11.

Pantelev, M. A., N. M. Dashkevich, and F. I. Ataulakhanov. 2015. Hemostasis and thrombosis beyond biochemistry: roles of geometry, flow and diffusion. *Thrombosis Research* 136: 699-711.

Peer, A., Ihmsen, M., Cornelis, J., Teschner, M. (2015). An implicit viscosity formulation for SPH fluids. *ACM Transactions on Graphics (TOG)*, 34(4), 114.

Physically viscous and non-viscous SPH modelling. *Astronomy & Astrophysics*, 403(2), 593-604.

Pimenta, L. C., Pereira, G. A., Michael, N., Mesquita, R. C., Bosque, M. M., Chaimowicz, L., Kumar, V. (2013). Swarm coordination based on smoothed particle hydrodynamics technique. *IEEE Transactions on Robotics*, 29(2), 383-399.

Ren, B., Fan, H., Bergel, G. L., Regueiro, R. A., Lai, X., Li, S. (2015). A peridynamics–SPH coupling approach to simulate soil fragmentation induced by shock waves. *Computational Mechanics*, 55(2), 287-302.

Rideout, V. C. (1991). *Mathematical and computer modeling of physiological systems* (p. 71). Englewood Cliffs, NJ:: Prentice Hall.

Riffert, H., Herold, H. (1995). Relativistic accretion disk structure revisited. *The Astrophysical Journal*, 450, 508.

Schulze, K. S. (2015). The imaging and modelling of the physical processes involved in digestion and absorption. *Acta Physiologica*, 213(2), 394-405.

Schütte, J., Hagemeyer, B., Holzner, F., Kubon, M., Werner, S., Freudigmann, C., Benz, K., Böttger, J., Gebhardt, R., Becker, H., Stelzle, M. (2011). “Artificial micro organs”—a microfluidic device for dielectrophoretic assembly of liver sinusoids. *Biomedical microdevices*, 13(3), 493-501

Sforza, D. M., Putman, C. M., Cebal, J. R. (2009). Hemodynamics of cerebral aneurysms. *Annual review of fluid mechanics*, 41, 91.

Shahriari, S., Maleki, H., Hassan, I., Kadem, L. (2012). Evaluation of shear stress accumulation on blood components in normal and dysfunctional bileaflet mechanical heart valves using smoothed particle hydrodynamics. *Journal of biomechanics*, 45(15), 2637-2644.

Šidlof, P., Horáček, J., Řidký, V. (2013). Parallel CFD simulation of flow in a 3D model of vibrating human vocal folds. *Computers & Fluids*, 80, 290-300.

Sigalotti, L. D. G., Klapp, J., Sira, E., Meleán, Y., Hasmy, A. (2003). SPH simulations of time-dependent Poiseuille flow at low Reynolds numbers. *Journal of computational physics*, 191(2), 622-638.

Simão, M., Ferreira, J. M., Mora-Rodriguez, J., Ramos, H. M. (2016). Identification of DVT diseases using numerical simulations. *Medical & biological engineering & computing*, 54(10), 1591-1609.

Sinnott M.D., Cleary P.W, Arkwright J.W, Dinning P.G.(2012) Investigating the relationships between peristaltic contraction and fluid transport in the human colon using Smoothed Particle Hydrodynamics *Comput Biol Med.* 42:492–503.

Springel, V. (2011). Smoothed particle hydrodynamics in astrophysics. arXiv preprint arXiv:1109.2219.

Springel, V., Hernquist, L. (2003). Cosmological smoothed particle hydrodynamics simulations: a hybrid multiphase model for star formation. *Monthly Notices of the Royal Astronomical Society*, 339(2), 289-311.

Stinson, G. S., Bailin, J., Couchman, H., Wadsley, J., Shen, S., Nickerson, S., Brook, C., Quinn, T. (2010). Cosmological galaxy formation simulations using smoothed particle hydrodynamics. *Monthly Notices of the Royal Astronomical Society*, 408(2), 812-826.

Tamamidis, P., Zhang, G., Assanis, D. N. (1996). Comparison of pressure-based and artificial compressibility methods for solving 3D steady incompressible viscous flows. *Journal of computational Physics*, 124(1), 1-13.

Topalović, M. D., Blagojević, M. R., Nikolić, A. V., Živković, M. M., Filipović, N. D. (2015, November). Application of smoothed particle hydrodynamics in biomechanics: Advanced procedure for discretization of complex biological shapes into pseudo-particles. In *Bioinformatics and Bioengineering (BIBE), 2015 IEEE 15th International Conference on* (pp. 1-4). IEEE.

- Van Ertbruggen, C., Hirsch, C., Paiva, M. (2005). Anatomically based three-dimensional model of airways to simulate flow and particle transport using computational fluid dynamics. *Journal of applied physiology*, 98(3), 970-980.
- Van Loon, R. (2010). Towards computational modelling of aortic stenosis. *International Journal for Numerical Methods in Biomedical Engineering*, 26(3 - 4), 405-420.
- Vassberg, J., Dehaan, M., Rivers, M., Wahls, R. (2008, August). Development of a common research model for applied CFD validation studies. In *26th AIAA Applied Aerodynamics Conference* (p. 6919).
- Verlet, L. (1967). Computer" experiments" on classical fluids. I. Thermodynamical properties of Lennard-Jones molecules. *Physical review*, 159(1), 98.
- Vogel, S. (1996). *Life in moving fluids: the physical biology of flow*. Princeton University Press.
- Von Neumann, J., Richtmyer, R. D. (1950). A method for the numerical computations of hydrodynamical shocks. *Journal of Mathematical Physics*, 21.
- Wijeratne, N. S., Hoo, K. A. (2008, June). Numerical studies on the hemodynamics in the human vein and venous valve. In *American Control Conference, 2008* (pp. 147-152). IEEE.
- Wootton, D. M., Ku, D. N. (1999). Fluid mechanics of vascular systems, diseases, and thrombosis. *Annual review of biomedical engineering*, 1(1), 299-329.

Wurm, M., Zeng, A. P. (2012). Mechanical disruption of mammalian cells in a microfluidic system and its numerical analysis based on computational fluid dynamics. *Lab on a Chip*, 12(6), 1071-1077.

Yang, X. F., Peng, S. L., Liu, M. B. (2014). A new kernel function for SPH with applications to free surface flows. *Applied Mathematical Modelling*, 38(15-16), 3822-3833.

Zervides, C., Narracott, A. J., Lawford, P. V., Hose, D. R. (2008). The role of venous valves in pressure shielding. *Biomedical engineering online*, 7(1), 8.

Zhang, J. N., Bergeron, A. L., Yu, Q., Sun, C., McIntire, L. V., López, J. A., Dong, J. F. (2002). Platelet aggregation and activation under complex patterns of shear stress. *Thrombosis and haemostasis*, 88(5), 817-821.